FISEVIER

Contents lists available at ScienceDirect

Quaternary Science Reviews

journal homepage: www.elsevier.com/locate/quascirev



Glacial isostatic adjustment near the center of the former Patagonian Ice Sheet (48°S) during the last 16.5 kyr



Matthias Troch ^{a,*}, Sebastien Bertrand ^a, Carina B. Lange ^{b, c, d}, Paola Cárdenas ^c, Helge Arz ^e, Silvio Pantoja-Gutiérrez ^b, Ricardo De Pol-Holz ^f, Rolf Kilian ^{g, h, 1}

- ^a Renard Centre of Marine Geology, Department of Geology, Ghent University, Gent, Belgium
- ^b Centro de Investigación Oceanográfica COPAS Sur-Austral and Departamento de Oceanografía, Universidad de Concepción, Concepción, Chile
- ^c Centro de Investigación Dinámica de Ecosistemas Marinos de Altas Latitudes (IDEAL), Universidad Austral de Chile, Valdivia, Chile
- ^d Scripps Institution of Oceanography, University of California San Diego, La Jolla, United States
- ^e Marine Geology, Leibniz Institute for Baltic Sea Research, Rostock-Warnemünde, Germany
- f Centro de Investigación GAIA-Antártica (CIGA) and Network for Extreme Environment Research (NEXER), Universidad de Magallanes, Punta Arenas, Chile
- g Department of Geology, University of Trier, Trier, Germany
- ^h Departamento de Biología Marina, Universidad de Magallanes, Punta Arenas, Chile

ARTICLE INFO

Article history: Received 4 October 2021 Received in revised form 15 December 2021 Accepted 17 December 2021 Available online 30 December 2021

Handling Editor: I Hendy

Keywords: Patagonia Isolation basin Sea level Salinity indicators Late glacial Holocene

ABSTRACT

Our understanding of glacial isostatic rebound across Patagonia is highly limited, despite its importance to constrain past ice volume estimates and better comprehend relative sea-level variations. With this in mind, our research objective is to reconstruct the magnitude and rate of Late Glacial and Holocene glacial isostatic adjustment near the center of the former Patagonian Ice Sheet. We focus on Larenas Bay (48°S; 1.26 km²), which is connected to Baker Channel through a shallow (7.4 m) and narrow (*ca.* 150 m across) inlet, and hence has the potential to record periods of basin isolation and marine ingression. The paleoenvironmental evolution of the bay was investigated through a sedimentological analysis of a 9.2 m long radiocarbon-dated sediment core covering the last 16.8 kyr. Salinity indicators, including diatom paleoecology, alkenone concentrations and CaCO₃ content, were used to reconstruct the bay's connectivity to the fjord. Results indicate that Larenas Bay was a marine environment before 16.5 cal kyr BP and after 9.1 cal kyr BP, but that it was disconnected from Baker Channel in-between. We infer that the postglacial rebound started before 16.5 cal kyr BP and that it outpaced global sea-level rise until slightly before 9.1 cal kyr BP. During the Late Glacial and early Holocene, the center of the former Patagonian Ice Sheet experienced an absolute uplift of ca. 96 m, at an average rate of 1.3 cm/yr. During the remainder of the Holocene, glacial isostatic adjustment continued (ca. 20 m), but at a slower average pace of 0.2 cm/yr. Comparisons between multi-millennial variations in the salinity indicators and existing records of global sea-level rise suggest that the glacial isostatic adjustment rate also fluctuated within these time intervals, likely in response to glacier dynamics. More specifically, most of the glacial isostatic adjustment registered between 16.5 - 9.1 cal kyr BP seems to have occurred before meltwater pulse 1A (14.5 - 14.0 kyr)BP). Likewise, it appears that the highest glacial isostatic rebound rates of the last 9.1 kyr occurred during the late Holocene, most likely in response to glacier recession from their Neoglacial maxima. This implies a relatively rapid response of the local solid earth to ice unloading, which agrees with independent modelling studies investigating contemporary uplift. We conclude that the center of the former Patagonian Ice Sheet experienced a glacial isostatic adjustment of ca. 116 m over the last 16.5 kyr, and that >80% occurred during the Late Glacial and early Holocene.

© 2021 Elsevier Ltd. All rights reserved.

Abbreviation: LGM, Last Glacial Maximum.

E-mail address: matthias.troch@ugent.be (M. Troch).

1. Introduction

Glacial isostatic adjustment is the vertical displacement of the solid earth in response to the growth and decay of ice sheets (Whitehouse, 2018). The magnitude and response time of such

^{*} Corresponding author.

¹ Deceased May 2019.

adjustments vary in both space and time, and mostly depend on the flexural rigidity of the lithosphere, viscosity of the mantle, and ice volume (Benn and Evans, 2010). In regions formerly covered by Pleistocene ice sheets, glacial isostatic rebound can trigger 100 m scale changes in relative sea level (Whitehouse, 2018). In addition, isostatic movements impact crustal stress distribution and the elevation-temperature feedback between glaciers and the atmosphere.

Observations of post-Last Glacial Maximum (LGM) glacial isostatic adjustment across Patagonia are scarce. The available reconstructions (Bourgois et al., 2016; Kilian et al., 2007; Ríos et al., 2020) and GPS measurements (Richter et al., 2016) suggest that postglacial isostatic rebound might have fluctuated considerably in both space and time. East of the Northern Patagonian Icefield, within the Lake General Carrera basin (Fig. 1), Bourgois et al. (2016) reconstructed glacial isostatic adjustment rates of 1.5 - 3.4 cm/yr for the past 7.9 kyr. These adjustment rates seem to decrease towards the south, with 0.4 - 0.5 cm/yr over the past 12.2 - 13 kyr near the Gulf of Sarmiento (52°S; Ríos et al., 2020), and 0.8 -0.9 cm/yr over the past 12.2 kyr near the eastern edge of the Gran Campo Nevado Icefield (53°S; Kilian et al., 2007). Furthermore, GPS observations made between 1996 and 2014 reveal contemporary glacial isostatic rebound rates >4 cm/yr in the north-central part of the Southern Patagonian Icefield (48.5 - 49.5°S; Richter et al., 2016). Quantifying these spatiotemporal variations more accurately is required to better constrain numerical models of past changes in the volume of the Patagonian Ice Sheet and ultimately estimate the contribution of the Patagonian Ice Sheet and of the contemporary glaciers to past, present and future global sea-level change (Bromwich and Nicolas, 2010; Clark and Tarasov, 2014). They are also needed to generate relative sea-level curves for southern Chile, which are almost inexistent (Garrett et al., 2020).

One way to reconstruct glacial isostatic adjustment is by analyzing sediment records from isolation basins. Isolation and marine ingression intervals can be identified by analyzing salinity indicators such as diatoms and alkenones, combined with tracers of environmental change, e.g., bulk organic geochemistry, biogenic carbonates, and sedimentation rates (Long et al., 2011; Ríos et al., 2020; Verleyen et al., 2017). Such an approach has proven successful to reconstruct past relative sea-level changes and glacial isostatic adjustment in, for example, Antarctica (Hodgson et al., 2016; Verleyen et al., 2017), Greenland (Long et al., 2011), New Zealand (Dlabola et al., 2015), Canada (Roe et al., 2013), Norway (Balascio et al., 2011) and Scotland (Mackie et al., 2007).

With this in mind, the objective of this study is to reconstruct the magnitude and rate of glacial isostatic adjustment near the center of the former Patagonian Ice Sheet during the Late Glacial and Holocene. We focus on Larenas Bay, which is connected to a marine-dominated fjord through a shallow inlet (SHOA, 2001) and is located near the center of the former Patagonian Ice Sheet (Fig. 1; Davies et al., 2020). As most isolation basins, Larenas Bay has the potential to have recorded isolation and marine ingression phases since its deglaciation. To reconstruct these phases and quantify glacial isostatic adjustment, we performed sedimentological and paleoecological analyses on a 9.2 m long radiocarbon dated sediment core.

2. Setting

Larenas Bay (48°S; 1.26 km²) is located along the northern shore of Baker Channel, which connects the Patagonian Andes in the east to the Pacific Ocean in the west (Fig. 1). Baker Channel and the parallel Martínez Channel to the north constitute the *ca.* 150 km long, west-east oriented, Baker-Martínez fjord system that separates the Northern from the Southern Patagonian icefields (Fig. 1a).

The Baker-Martínez fjord system reaches depths of 1075 m b.s.l. (Piret et al., 2019).

The deglaciation of the Baker-Martínez fjord system started 18 – 17 kyr ago, when the Patagonian Ice Sheet (38 – 56°S) started to recede from its calving position at the continental shelf edge (Fig. 1a; Davies et al., 2020; Hubbard et al., 2005). Its final opening resulted in the gradual separation of the Patagonian Ice Sheet into the Northern and Southern Patagonian icefields between 12.6 and 11.7 kyr BP and allowed the drainage of the great Patagonian glacial paleolakes General Carrera and Cochrane into the Pacific Ocean (Fig. 1a; Thorndycraft et al., 2019). Modelling studies suggest that the Northern and Southern Patagonian icefields reached their present-day configuration by *ca.* 11 kyr BP (Fig. 1a; Hubbard et al., 2005), which is supported by geomorphological data (Davies et al., 2020). Minor glacier advances occurred during the Neoglacial period (Aniya, 2013).

The Baker-Martínez fjord system has a hyperhumid maritime climate (Garreaud et al., 2013), and it receives freshwater and sediment from four glacier-fed rivers, i.e., Baker, Pascua, Huemules and Bravo, and from Jorge Montt Glacier (Fig. 1a). Its water column has a two-layer structure with outflowing (westward) estuarine water in the upper 5 - 30 m and inflowing (eastward) oceanic water below (Aiken, 2012; Sievers and Silva, 2008). The cold surface layer results from river runoff and meltwater input, and is characterized by low salinity (<31 PSU) and high turbidity (>10 NTU) values (Aiken, 2012; Quiroga et al., 2016; Rebolledo et al., 2019). Its thickness and extent vary spatially and seasonally, which results in a pycnocline located between 5 and 30 m depth (Aiken, 2012: González et al., 2013). The warmer oceanic waters below the pvcnocline originate in the Southern Ocean and are characterized by high salinity (>31 PSU) and low turbidity (<1 NTU) values (Quiroga et al., 2016; Rebolledo et al., 2019). Phytoplankton is limited to the upper 25 m of the water column and its abundance increases oceanwards (Quiroga et al., 2016; Rebolledo et al., 2019). In the outer, more marine sections of the Baker-Martínez fjord system, the phytoplankton is dominated by diatoms (González et al., 2013). The main sedimentation process consists in suspension fallout from the turbid surface layer (DaSilva et al., 1997; Rebolledo et al., 2019). Settling of ice-rafted debris also occurs in the vicinity of calving glacier fronts (Dowdeswell and Vásquez, 2013), which were more abundant and closer to Larenas Bay during the deglaciation (Fig. 1a; Davies et al., 2020).

The main feature of Larenas Bay is its connection to Baker Channel via a narrow (ca. 150 m across) and shallow inlet at its southeastern end (Fig. 1b; SHOA, 2001). Depending on surface and tidal currents, sediments entrained by the hypopycnal plume in Baker Channel might reach Larenas Bay. The Larenas Bay watershed has an area of 6.78 km² (Fig. 1b) and its vegetation is dominated by native *Nothofagus* rainforests (Luebert and Pliscoff, 2006). Herbs, shrubs, ferns, and peatlands only have a minor occurrence, and plants using the C₄ photosynthetic pathway are virtually absent (Luebert and Pliscoff, 2006). The bay's shoreline is surrounded by $10-20^{\circ}$ slopes.

Chilean Patagonia has a unique tectonic setting with a thin lithosphere and low effective viscosity of the asthenosphere and upper mantle (Lagabrielle et al., 2004; Richter et al., 2016). This mainly results from an oceanic ridge collision about 3 Ma ago, which created an asthenospheric slab window below the icefields (Georgieva et al., 2016; Lagabrielle et al., 2004). Active subduction is present *ca.* 180 km west of Larenas Bay, with the Chile Triple Junction (46°S) being its prime feature. At this junction, the Nazca and Antarctic plates, separated by the Chile Ridge, subduct below the South America plate (Lagabrielle et al., 2004) at a convergence rate of 66 mm/yr and 18.5 mm/yr, respectively (Wang et al., 2007). Part of this convergence has been accommodated by the Liquiñe-

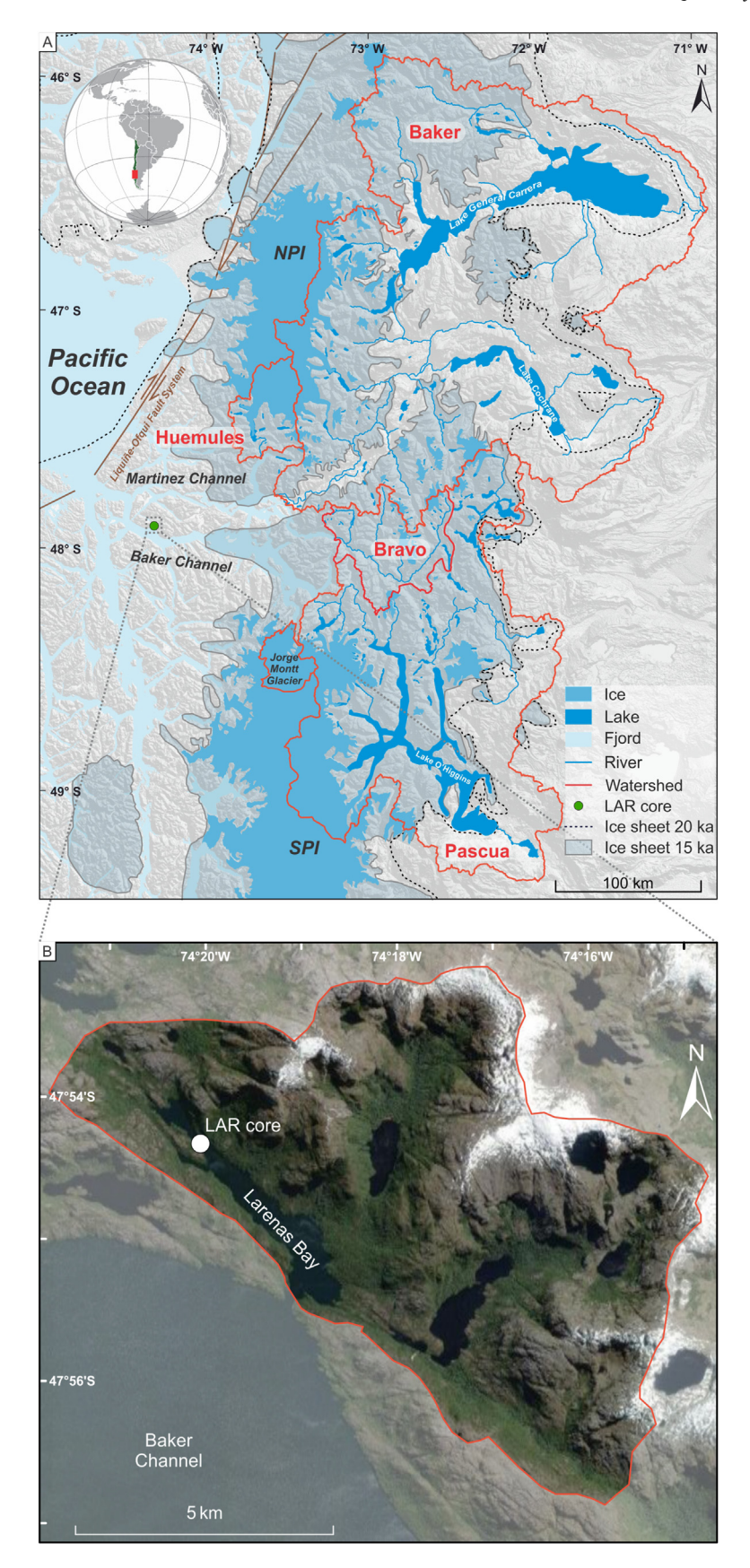


Fig. 1. Location of Larenas Bay, along Baker Channel, in Chilean Patagonia. (a) Overview of the late Quaternary Patagonian Ice Sheet evolution (Davies et al., 2020), tectonic features (Cembrano et al., 2002) and watersheds affecting the study area. NPI = Northern Patagonian Icefield. SPI = Southern Patagonian Icefield. (b) Satellite image of the Larenas Bay watershed with the position of the LAR core (Esri World Imagery).

Ofqui Fault System (Fig. 1a; Cembrano et al., 2002).

3. Material and methods

3.1. Bathymetry, sub-bottom profiles, CTD, and sediment coring

The bathymetry and sub-bottom stratigraphy of Larenas Bay were investigated with a Parametric Echo Sounding System SES 96 from Innomar (Wunderlich and Müller, 2003). Both the high (100 kHz) and low (12 kHz) frequency data were processed using the ISE software version 2.9.5 (Innomar.com). Water depths were determined from the high frequency signal and an acoustic velocity of 1475 m/s (Chen and Millero, 1977) following Praet et al. (2017). The sub-bottom stratigraphy was visualized from the low frequency signal in the IHS Kingdom Suite software. Eight vertical CTD profiles were taken with an RBR Maestro, operating at a sampling rate of 6 Hz, during austral summer 2021. CTD data were plotted using Ocean Data View version 5.4.0 (Schlitzer, 2021).

The LAR sediment core (47.905467°S, 74.334233°W) was collected with a 5 m long Uwitec piston corer (63 mm diameter) onboard of the R/V Gran Campo II on September 12, 2008. Two overlapping ~4.7 m long piston cores (LAR I and LAR II) and a 65 cm long gravity core that preserved the sediment-water interface were retrieved. The gravity and piston cores were correlated using high-resolution (1 mm) magnetic susceptibility data, resulting in a composite core length of 9.20 m. All core depths mentioned in this article are composite depths. To investigate modern sediments, the top centimeter of a Rumohr gravity core (LAR R2) taken at the same location on January 19, 2020 was used.

The piston cores were sampled in 2 cm thick slices, which were subsequently weighed and freeze-dried. Discrete analyses were performed at a 10-20 cm interval. In addition, wet and dry bulk density were measured on 1 cm thick slices $(2.9\pm0.7~\text{cm}^3)$ every 20 cm. The LAR sediment core was correlated to the sub-bottom stratigraphy by linking changes in wet bulk density to high-amplitude seismic reflections.

3.2. Magnetic susceptibility

Continuous high-resolution logging of magnetic susceptibility was accomplished using a Bartington MS2E spot sensor integrated into an automatic logging system (Nowaczyk, 2002). Measurements were performed on the split cores in steps of 1 mm with drift correction every 10 mm using readings in air. All magnetic susceptibility measurements reported in this article are volume-specific.

3.3. Bulk organic geochemistry

The total organic carbon content and stable carbon isotope composition (δ^{13} C) of the bulk organic matter were analyzed at the UC Davis Stable Isotope Facility. Optimal sample weight (7-60 mg)was determined by estimating the organic matter content via losson-ignition at 550°C (Heiri et al., 2001). Samples were treated with 60 μ L of sulfurous acid (6 - 8%) to remove inorganic carbon (Verardo et al., 1990). Measurements were performed with an elemental analyzer (Elementar Vario EL Cube) interfaced with a continuous flow isotope ratio mass spectrometer (PDZ Europa 20-20). The $\delta^{13}\text{C}$ precision, calculated as the mean standard deviation of replicate analyses of internal standards, was 0.03%. The relative contributions of terrestrial and marine organic carbon were calculated using the $\delta^{13}C$ data and the end-members of Bertrand et al. (2012b) and Hebbeln et al. (2000) following Rebolledo et al. (2019). The organic matter content was calculated by multiplying the total organic carbon content by a factor 2.2.

3.4. Biogenic silica

The biogenic silica concentration was measured using the alkaline extraction technique as described in Bertrand et al. (2012b), which was in turn adapted from Carter and Colman (1994) and Mortlock and Froelich (1989). Biogenic silica was extracted from the sediment samples using 0.2 N NaOH after removing organic matter and carbonates with 10% H₂O₂ and 1 N HCl. The extracts were analyzed for Si and Al by Inductively Coupled Plasma-Atomic Emission Spectrometry (Varian 720-ES). Dissolution of lithogenic silica was corrected using the measured Al concentration: biogenic silica = measured Si - 2 x Al. This correction assumes that all extracted Al originates from the lithogenic fraction (Bertrand et al., 2012b). The analytical precision on the biogenic silica values was 0.15 wt%. The biogenic opal content was calculated by multiplying the biogenic silica content by a factor 2.4 (Mortlock and Froelich, 1989).

3.5. Calcium carbonate

The inorganic carbon content was analyzed using an UIC CM5017 coulometer equipped with a CM5330 acidification module. For each sample, approximately 50 mg of sediment was precisely weighed (0.1 mg) into a reaction flask. $\rm H_3PO_4$ (5 mL, 2 N) was used to release the $\rm CO_2$ from the inorganic carbon. The amount of $\rm CO_2$ was subsequently measured through absolute coulometric titration. This method assumes that 100% of the measured $\rm CO_2$ originates from the dissolution of calcium carbonate. The $\rm CaCO_3$ content was calculated by multiplying the inorganic carbon content by a factor 8.33. The analytical precision and detection limit were 6.2% and 0.001 wt% $\rm CaCO_3$, respectively.

3.6. Lithogenic fraction

The weight percentage of the lithogenic fraction of the sediment was calculated as: lithogenic fraction (wt%) = 100 - organic matter (wt%) – biogenic opal (wt%) – $CaCO_3$ (wt%) (Bertrand et al., 2012b).

3.7. Grain size

Grain size was determined on the terrigenous fraction of the sediment. Measurements were performed with a Malvern Mastersizer 3000 laser diffraction particle size analyzer equipped with a Hydro MV dispersion unit. To isolate the terrigenous fraction, samples were treated with boiling $\rm H_2O_2$ (2 mL, 30%), HCl (1 mL, 10%), and NaOH (1 mL, 2 N), to remove organic matter, carbonates, and biogenic silica, respectively. The samples were then boiled with (NaPO₃)₆ (1 mL, 2%) to ensure complete disaggregation of the particles and continuous ultrasounds (10%) were used during analysis. A stirrer (2500 rpm) kept the samples in suspension. Grain-size distributions were measured three times during 12 s and the geometric mean was calculated using GRADISTAT v8 (Blott and Pye, 2001).

The weight percentages of the lithogenic fractions >63 μm and >150 $\,\mu m$ were analyzed through wet sieving. Five (30.5 - 680.5 cm) or 10 g (680.5 - 910.5 cm) of freeze-dried sediment was used for analysis. Organic matter was removed through loss-onignition by heating the samples in a muffle furnace at 750°C for 4 h. Inorganic carbon and biogenic silica were removed with acetic acid (5 mL, 100%) and boiling NaOH (5 mL, 2 N), respectively.

3.8. Alkenones

Sediment samples (ca. 4 g) were homogenized, freeze-dried and spiked with n-heptacosanone as a recovery standard. Lipids were

extracted using methanol followed by methanol and methylene chloride (1:3) in an ultrasonication bath. After each extraction, samples were centrifuged and both supernatants were combined and dried under a N₂ stream (Bligh and Dyer, 1959). Extracts were separated by column chromatography in a Pasteur pipette with activated silica and the fraction containing C₃₇ alkenones was dried and re-dissolved in isooctane adding 5-alphacholestane as internal standard. Gas chromatography was performed on an Agilent 6890 instrument connected to a flame ionization detector. Alkenone separation and determination was achieved with a fused silica capillary column (30 m length, i.d. = 0.25 mm HP5-MS, film thickness = $0.25 \mu m$) with automated injection. The oven temperature was programmed to rise to 50°C in 1 min, then to 120°C at 30°C/min, then to 300°C at 6°C/min and held for 40 min. Helium was used as a carrier gas (16.91 psi) with a flow of 2 mL/min. C₃₇ alkenones were identified by comparison with alkenone retention times of Emiliania huxleyi cultures. Alkenones were quantified using calibration curves with 5-alphacholestane, and the total alkenone contents were calculated as the sum of di-, tri- and tetraunsaturated C₃₇ alkenones and expressed in ng/g. Detection limit for individual C₃₇ alkenones was 5 ng/g.

3.9. Diatom paleoecology

Smear slides were prepared following the IODP digital reference (Marsaglia et al., 2013, 2015), and analyzed with a Zeiss Axioskop 2 Plus microscope at 400X magnification. Diatoms were identified to species or species group level, and classified by their ecological affinity into marine and freshwater categories. Subsequently, we focused on estimating the percentages of marine and freshwater diatoms by using the chart for visual percentage estimation defined by Mazzullo and Graham (1988).

3.10. Core chronology

Radiocarbon ages were determined on nine organic (plant remains) and three inorganic (mollusk shells) samples via accelerated mass-spectrometry at NOSAMS (Woods Hole Oceanographic Institution, USA) or at the Department of Earth Systems Sciences of the University of California (Irvine, USA) (Table 1). All radiocarbon ages were calibrated using the SHCal20 calibration curve (Hogg et al., 2020), except for the mollusk sample (OS-74689) at 610.5 cm depth (Marine20 curve; Table 1; Heaton et al., 2020). The oldest two mollusk samples (OS-74691 and OS-74692) were calibrated using the SHCal20 curve as freshwater conditions prevailed during the Late Glacial. The age-depth model and sedimentation

rates were calculated using the BACON 2.4.3 software (Blaauw and Christen, 2011) in R (R Core Team, 2020).

4. Results

4.1. Bathymetry

Larenas Bay has a relatively flat basin morphology, and it is separated from Baker Channel by a shallow sill (7.4 m depth) (Fig. 2). Its maximum water depth of 44 m (Fig. 2) is in strong contrast to the ~700 m deep adjacent Baker Channel (Piret et al., 2019). The bay is divided into two sub-basins. The main sub-basin is located at 32-44 m depth, and the smaller one at the northwestern end of the bay at 22-25 m. The Larenas sediment core was retrieved from the northwestern sub-basin at a water depth of 24 m (Fig. 2).

4.2. Water column

A two-layered structure was observed within the water column of Larenas Bay during austral summer 2021 (Fig. 2b). The upper water column (0-5 m) was relatively warm $(12.5-14.4^{\circ}\text{C})$ and had a particularly low salinity (<20 PSU). A consistent decrease in water temperature and increase in salinity occurred with depth, to reach ca. 9.8°C and 31.3 PSU at 41 m (Fig. 2b). Two turbidity maxima (>3 NTU) were observed in the upper 5 m of the water column, one around stations A and B in the northwestern end of the bay and the second across the connection between Baker Channel and Larenas Bay (Fig. 2b). Similar turbidity maxima were also observed in the deepest parts of the bay (Fig. 2b).

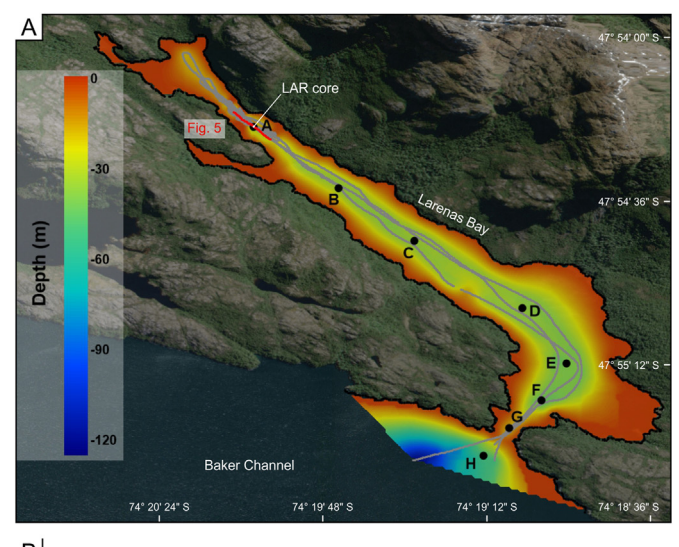
4.3. Lithology and chronology

Four different lithological units can be recognized in the LAR sediment core (Fig. 3). The bottom Unit I consists of sandy mud with occasionally some gravel and has a light grey color. Units II and III consist of sandy mud and have a brown and black color, respectively. Unit III is the most organic of the entire core. Unit IV consists of very fine silt with some discrete coarser grained layers (<3.5 cm thick) and has a grey color, but it is overall darker than the bottom unit (Fig. 3).

According to the age-depth model, the LAR sediment core covers the last 16.8 kyr (Fig. 3). Throughout this period, the sedimentation rate varied considerably, from 9.6 mm/yr during the Late Glacial (Unit I), over 0.1-0.3 mm/yr across the Late Glacial — Holocene transition (units II and III), to 0.7 mm/yr during the Holocene (Unit

Table 1
Radiocarbon ages obtained on the LAR sediment core. UCI = Department of Earth Systems Sciences of the University of California (Irvine, CA, USA). OS = National Ocean Sciences Accelerator Mass Spectrometry Facility (NOSAMS) of the Woods Hole Oceanographic Institution (Woods Hole, MA, USA). The radiocarbon age obtained on the wood sample at 66.0 cm depth was considered as an outlier (Fig. 4) since the grain-size and magnetic susceptibility data indicate that its deposition might be related to the coarse detrital layer observed at *ca.* 70 cm depth (Fig. 3). SHCal20 = Southern Hemisphere 2020 calibration curve (Hogg et al., 2020). Marine20 = Marine 2020 calibration curve (Heaton et al., 2020).

Core	Sample depth (cm)	Composite depth (cm)	Laboratory code	Material	δ^{13} C (‰)	14 C yr BP ($\pm 1\sigma$)	Calibration curve	2σ range calibrated ages (cal. yr BP)
LAR I	46.5	66.0	UCI-108153	Wood	_	1620 ± 15	SHCal20	1416-1528
LAR I	120.0	139.5	UCI-108154	Nothofagus sp. leaf	_	2060 ± 15	SHCal20	1926-2010
LAR I	215.0	234.5	UCI-108155	Wood	_	3120 ± 20	SHCal20	3211 - 3371
LAR I	321.0	340.5	UCI-108156	Wood	_	4185 ± 20	SHCal20	4572 - 4827
LAR I	434.0	453.5	UCI-108157	Wood	_	5505 ± 20	SHCal20	6199 - 6310
LAR II	544.0	571.5	OS-74688	Plant/wood	-25.55	7040 ± 45	SHCal20	7706 – 7936
LAR II	583.0	610.5	OS-74689	Marine mollusk shell	-3.92	8150 ± 45	Marine20	8302 - 8612
LAR II	654.0	681.5	OS-74690	Plant/wood	-29.73	9590 ± 65	SHCal20	10,664 - 11,165
LAR II	681.0	708.5	OS-157727	Plant/wood	-28.94	$12,100 \pm 90$	SHCal20	13,754 - 14,178
LAR II	689.0	716.5	OS-157728	Plant/wood	-28.62	$12,200 \pm 90$	SHCal20	13,794 - 14,798
LAR II	750.0	777.5	OS-74691	Marine mollusk shell	1.4	$13,800 \pm 65$	SHCal20	16,437 - 16,961
LAR II	843.0	870.5	OS-74692	Marine mollusk shell	0.63	$13,900 \pm 60$	SHCal20	16,609 — 17,034



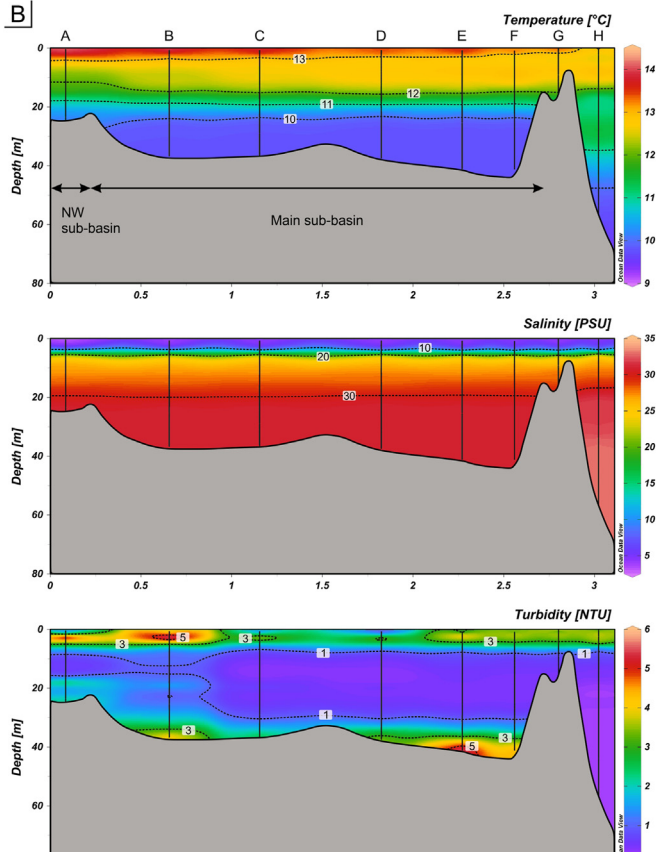


Fig. 2. Bathymetry and hydrography of Larenas Bay. (a) Bathymetric map of Larenas Bay with the survey lines indicated in grey, and location of the CTD stations investigated during summer 2021 (Esri World Imagery in the background). (b) CTD data plotted using Ocean Data View (Schlitzer, 2021).

1.5 Section Distance [km]

IV; Fig. 3).

4.4. Sediment composition

Within the bottom Unit I, the lithogenic fraction prevails $(96.94 \pm 1.02 \text{ wt\%}; \text{ Fig. 4})$. The amount of organic matter $(0.82 \pm 0.66 \text{ wt\%})$, biogenic opal $(2.02 \pm 0.54 \text{ wt\%})$, and CaCO₃

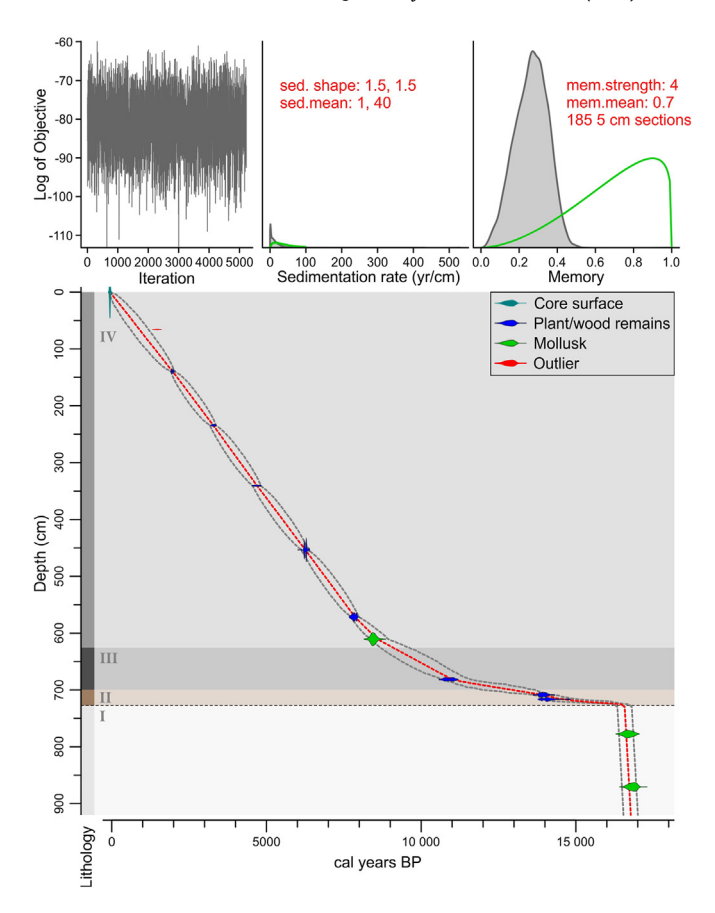


Fig. 3. Core lithology and age-depth model of the LAR sediment core produced with the BACON 2.4.3 software. The upper panels depict the Markov Chain Monte Carlo iterations (left panel), and the prior (green curves) and posterior (grey histograms) distribution of the sedimentation rate (middle panel) and memory (right panel). The lower panel shows the calibrated ¹⁴C dates and the age-depth model. The probability distribution of the calibrated ¹⁴C ages is indicated in blue (plant/wood remains), green (mollusk) or red (outlier). The 95% confidence interval of the age-depth model is indicated by the grey dashed lines, the mean age of the model is shown with the dashed red line. The dashed horizontal line between units I and II represents a boundary across which the memory strength and mean settings of the model are reset. The core lithology is presented to the left and as semi-transparent rectangles in the background. (For interpretation of the references to color in this figure legend, the reader is referred to the Web version of this article.)

 $(0.25\pm0.38~\text{wt\%})$ is low, whereas magnetic susceptibility (147 \pm 54 \cdot 10⁻⁵ S.l.), mean grain size (14.89 \pm 6.92 μ m) and the proportion of lithogenic particles >63 μ m and >150 μ m (13 \pm 11 and 4 \pm 9 wt%, respectively) are high but very variable (Fig. 4). The average δ^{13} C value ($-24.20\pm0.57\%$) indicates that the proportions of marine (45 \pm 7%) and terrestrial (55 \pm 7%) organic matter are nearly equal. Alkenones could not be quantified between 730 and 800 cm due to the presence of steryl-alkyl ether (Wang et al., 2019), and their abundance is high, but variable, in the rest of Unit I (288 \pm 142 ng/g). The diatom content is overall low (4 \pm 3%) and dominated by marine species (97 \pm 4%). Between 730 - 755 cm and 880 - 920 cm depth, only fragments of diatom frustules were observed (Fig. 4).

Across units II and III, both the organic matter (15.50 \pm 8.53 wt %) and biogenic opal (7.64 \pm 5.05 wt%) contents increase and peak at 672.5 cm and 642.5 cm, respectively. However, CaCO₃ remains virtually absent (<0.03 wt%; Fig. 4). Magnetic susceptibility remains below 135 \cdot 10⁻⁵ S.I., except for a peak between 689.6 and 675.5 cm. Mean grain size (16.21 \pm 9.89 μ m) and the proportion of lithogenic particles >63 μ m remain similar (11 \pm 8 wt%) to what is observed below, but the lithogenic fraction >150 μ m decreases

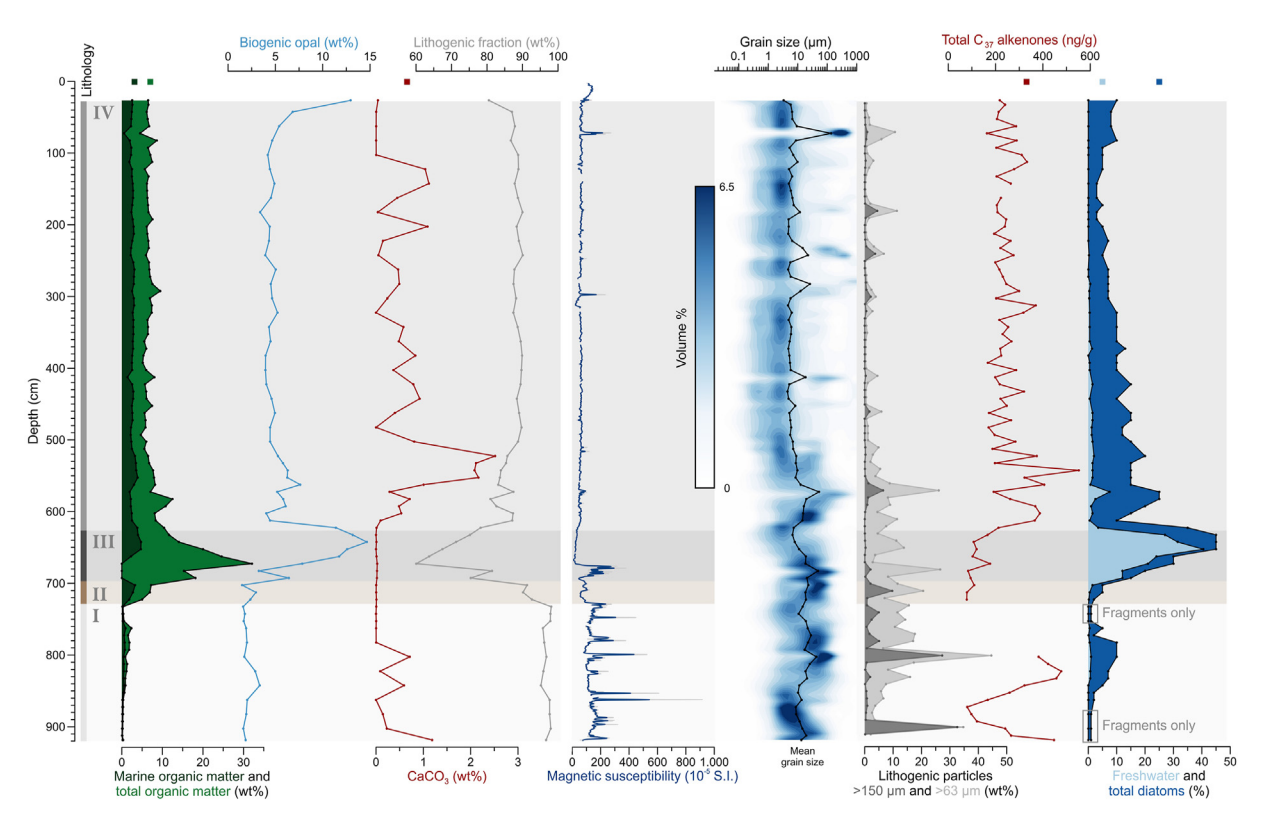


Fig. 4. Geochemical and physical parameters, and diatom paleoecology, measured on the LAR sediment core and modern sediment sample (indicated by the square symbols). For the high-resolution magnetic susceptibility measurements, the raw data (1 mm resolution) are presented in grey and the blue curve corresponds to the running average over 1 cm (11 data points). The core lithology is presented to the left and as semi-transparent rectangles in the background. Alkenones could not be quantified at 150 cm and between 730 and 800 cm depth due to the presence of steryl-alkyl ether (Wang et al., 2019). Between 730 – 755 cm and 880 – 920 cm depth, only fragments of diatom frustules were observed. (For interpretation of the references to color in this figure legend, the reader is referred to the Web version of this article.)

significantly (2 \pm 3 wt%; Fig. 4). The average δ^{13} C value ($-26.13 \pm 1.65\%$) indicates that organic matter is predominantly terrestrial (78 \pm 18%). The average alkenone content decreases to 112 \pm 34 ng/g, and the average diatom content increases to 24 \pm 17%. Freshwater diatom species become important in Unit II (17 \pm 12%) and prevail in Unit III (73 \pm 11%; Fig. 4).

Within Unit IV, the organic matter and biogenic opal content decrease and stabilize at intermediate values (6.84 ± 1.38 wt% and 5.30 ± 1.92 wt%; Fig. 4). The CaCO₃ content varies at a relatively high frequency between 570 and 110 cm (0.81 \pm 0.72 wt%) but it is nearly absent above 110 cm (<0.05 wt%). The lithogenic fraction and magnetic susceptibility stabilize at 87.02 \pm 2.92 wt% and 63 \pm 17 \cdot 10^{-5} S.I. The base of Unit IV (625 – 560 cm depth) is relatively coarse grained, with a lithogenic fraction >63 µm and mean grain size of 11 \pm 7 wt% and 16.64 \pm 12.66 μ m. Above, lithogenic particles >63 μ m are nearly absent (1 \pm 1 wt%), and mean grain size stabilizes at $5.22 \pm 1.27 \, \mu m$, except for some discrete peaks (Fig. 4). The average $\delta^{13} C$ value of $-24.65 \pm 0.69\%$ indicates that organic matter mostly originates from terrestrial plants (61 \pm 9%). The alkenone content is high, but variable (256 \pm 71 ng/g). The diatom content decreases to an average of 11 ± 7 wt% with a dominance of marine species (95 \pm 6%; Fig. 4).

The modern sediment sample contains 7.03 wt% organic matter and 0.66 wt% CaCO₃. The alkenone content is 331 ng/g and the sample contains 25% diatoms, which are dominated by marine species (80%). The δ^{13} C value of -24.21% indicates that the proportions of marine (45%) and terrestrial (55%) organic matter are nearly equal (Fig. 4).

4.5. Sub-bottom stratigraphy

The seismic reflectors within the northwestern sub-basin of Larenas Bay indicate a sub-horizontal stratification which gradually steepens towards the northwest (Fig. 5a). A transparent seismic facies with chaotic discontinuous reflectors, most likely representing a mass-transport deposit, is present towards the southeast of the coring location at a depth of 36.5-38.6 ms two-way-travel time. Bedrock was reached at a variable depth (29.0-49.5 ms two-way-travel time) across the sub-basin and the sedimentary infill reached a maximum observed thickness of 19.9 ms two-way-travel time.

4.6. Core-to-seismic correlation

We focused on correlating the main reflector in the seismic profile to a marked change in wet bulk density in the core (Fig. 5). As the main reflector separates a dense seismic facies below from a transparent seismic facies above, we infer that wet bulk density must decrease upwards, which allows us to correlate this reflector with a sharp lithological boundary between lithological units I and II. This correlation is based on the stronger influence of sharp, lithological boundaries on acoustic impedance, and thus seismic reflection magnitude, than gradual transitions (Reynolds, 2011, Fig. 5).

This core-to-seismic correlation results in an apparent average acoustic velocity of 1346 m/s along the sedimentary infill of Larenas Bay, which is in agreement with velocities observed in Chilean fjord sediments (1130-1475 m/s; Piret et al., 2018; Wils et al., 2018). From this apparent velocity, the inferred thickness of the

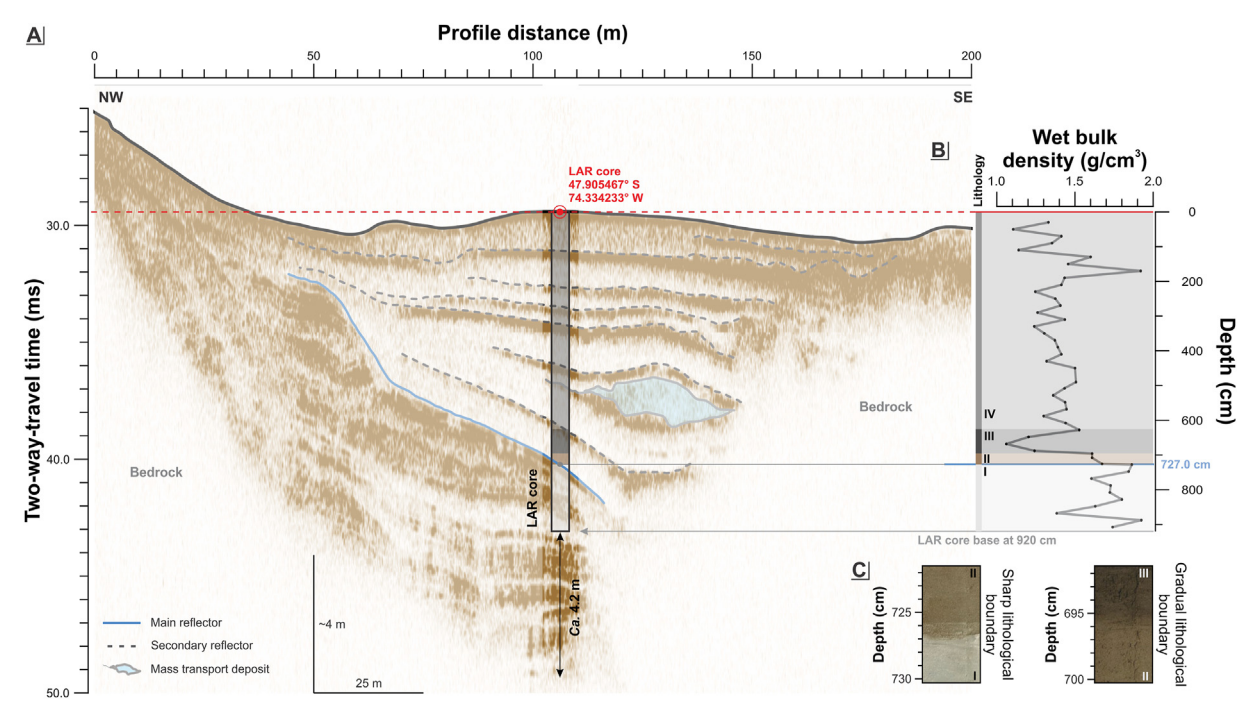


Fig. 5. Core-to-seismic correlation. (a) Sub-bottom profile of the northwestern sub-basin of Larenas Bay (see Fig. 2 for location) with indication of the main seismic reflector (blue line). The LAR sediment core is projected on the profile (black rectangle). (b) Sediment core lithology and wet bulk density. (c) Optical images of lithological boundaries across which an upward decrease in wet bulk density occurs. The average acoustic velocity resulting from this core-to-seismic correlation is 1346 m/s. (For interpretation of the references to color in this figure legend, the reader is referred to the Web version of this article.)

sedimentary infill in the northwestern sub-basin of Larenas Bay is at least 13.4 m, of which the lower 4.2 m was not sampled by the LAR sediment core (Fig. 5a).

5. Discussion

5.1. Modern hydrographic conditions

In its present-day configuration, Larenas Bay is connected with Baker Channel through a narrow and relatively shallow inlet (Fig. 2a). Hydrographic data show that the bay's water masses are essentially the same as those of the adjacent fjord, suggesting that a 7.4 m deep inlet is sufficient for the bay to be fully marine, despite the fjord stratification (Fig. 2b). A 7.4 m deep sill allows the inflow of both surficial brackish waters and that of deeper ocean waters into the bay. This most likely reflects the relatively thin (\sim 5 m) brackish surface layer so far west in Baker Channel, especially in winter (Quiroga et al., 2016; Rebolledo et al., 2019). It is likely that once the sill reaches a depth of 0 \sim 5 m, only the surface brackish water can enter the bay, resulting in intermediate salinity conditions.

5.2. Sedimentological interpretation

The geochemical, physical, and biological parameters presented in Fig. 4 primarily reflect past changes in ecology, sediment sources and erosion processes within Larenas Bay and its watershed. Within the scope of this study, we focus on paleosalinity and paleoenvironmental indicators to investigate the connectivity between Larenas Bay and Baker Channel over the past 16.8 kyr (Fig. 6). The presence of CaCO₃ in the bay's sediments is used as an indicator of marine waters flowing into the bay, as carbonate rocks are virtually absent in the surrounding watersheds (Fig. 1a; SERNAGEOMIN, 2003). Detrital carbonates are therefore negligible

and virtually all CaCO₃ originates from biological production in the Baker-Martínez fjord system (Rebolledo et al., 2019). Diatom paleoecology and alkenone content are used as salinity indicators because of the particular salinity preferences of different diatom taxa and alkenone producers (Bendle et al., 2009; Long et al., 2011; Rebolledo et al., 2019). It is however important to note that none of these salinity indicators provide quantitative reconstructions of salinity, since bioproductivity also varies with climate, water temperature and turbidity, nutrient availability, etc. (Aracena et al., 2015; Ríos et al., 2020). The mostly marine conditions that currently characterize Larenas Bay are well represented in the marine and salinity indicators measured on the modern sediment sample (Fig. 6). The proportion of marine diatoms (80%) is particularly high, and both carbonates (0.66 wt% CaCO₃) and alkenones (331 ng/g) are abundant. Such values in the sediment core therefore indicate that the sill was submerged and that marine waters could enter Larenas Bay, offering a reference point to interpret the sediment record.

In addition to these salinity indicators, the sedimentation rate, the accumulation rate of terrestrial organic carbon, the weight percentage of lithogenic particles >63 µm and >150 µm, and mean grain size are used to reconstruct the paleoenvironmental evolution of Larenas Bay and its watershed (Fig. 6). The sedimentation rate represents the input of sediments from both the local watershed and Baker Channel, whereas the accumulation rate of terrestrial organic carbon mostly reflects vegetation density in, and sediment supply from, the local watershed (Fig. 1b). The sediments transported in Baker Channel are relatively poor in terrestrial organic carbon (Rebolledo et al., 2019) and therefore contribute very little to its accumulation in Larenas Bay. In proglacial environments, the proportions of lithogenic particles >63 µm and >150 µm are generally used to indicate the presence of ice-rafted debris (Bertrand et al., 2017). In the Holocene sediments of Larenas Bay, however, they mostly represent the transport of loose

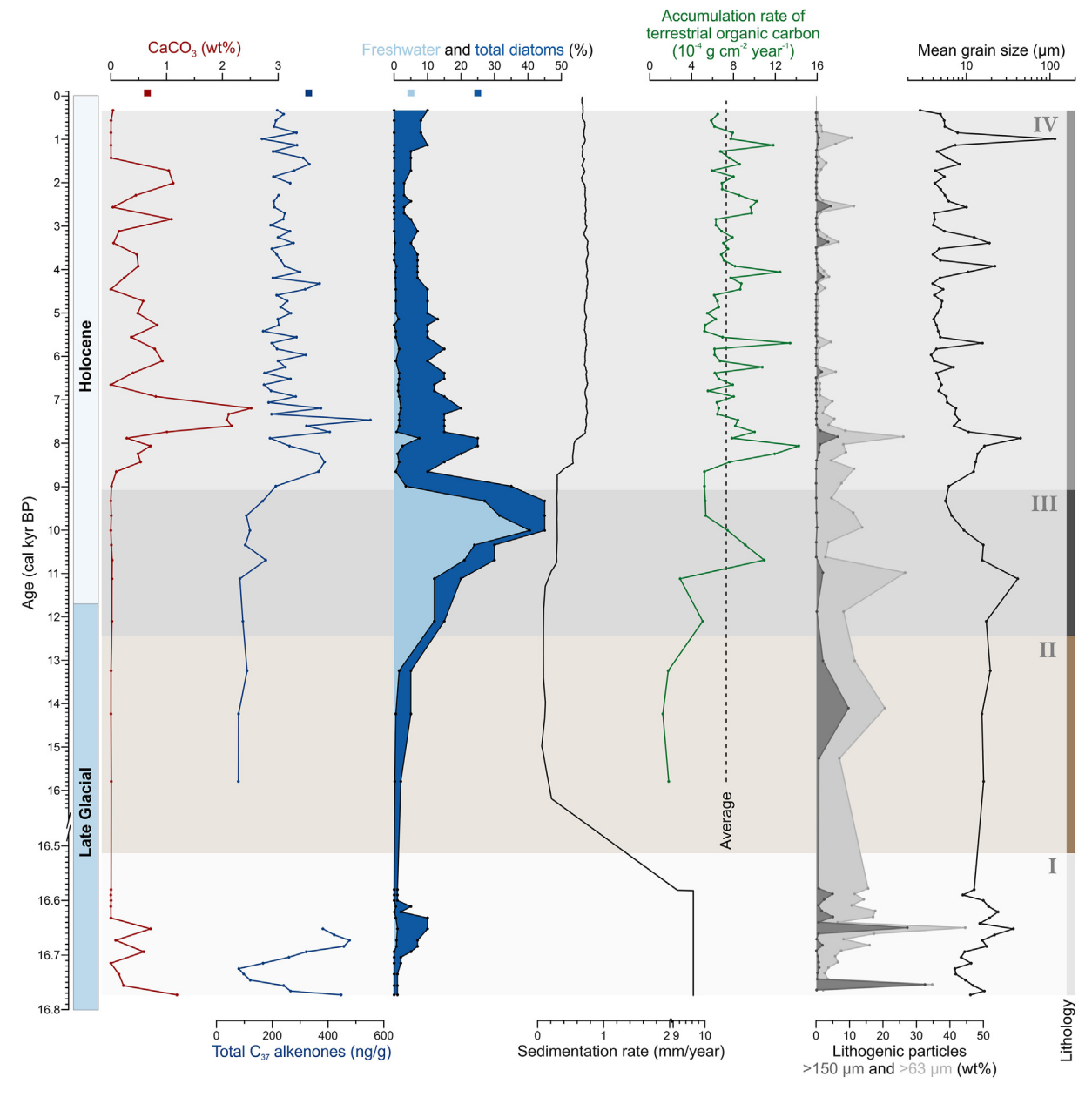


Fig. 6. Salinity and paleoenvironmental indicators versus age. The modern sediment sample is indicated by the square symbols. The core lithology is presented to the right and as semi-transparent rectangles in the background. The accumulation rate of terrestrial organic carbon for unit I is not presented as the high but poorly resolved sedimentation rates over this unit (9.6 mm/year; Fig. 3) overamplify any minor change in organic carbon content (0.37 \pm 0.30 wt%).

detrital material from the bare slopes surrounding Larenas Bay induced by run-off, slope failure, floods and/or seismic activity (Lasher et al., 2020; Wils et al., 2018). Variations in mean grain size mainly result from changes in sediment source(s) and erosion and transport processes.

5.3. Paleoenvironmental reconstruction

The sediments at the bottom of the LAR core (>900 cm) have an age of 16.8 cal kyr BP (Fig. 3) and consist mainly of relatively coarse (13.21 \pm 2.77 μm) lithogenic material (97.29 \pm 0.92 wt%) rich in icerafted debris (Fig. 4). We interpret that these sediments were deposited in a glacier-proximal environment (Bertrand et al., 2017; DaSilva et al., 1997). As the core did not penetrate the entire

sedimentary infill of the bay, the deglaciation of Larenas Bay must have occurred before 16.8 kyr. From the sub-bottom profile (Fig. 5), we know that at least 4.2 m of sediment was not cored and that no major sedimentological changes occurred during this interval, which, based on the extrapolation of the 9.6 mm/yr sedimentation rate (Fig. 3), represents 0.4 kyr. Therefore, we propose 17.2 kyr as the minimum age of the deglaciation of Larenas Bay. This age is in agreement with the retreat of the Patagonian Ice Sheet from a position at the western end of Baker Channel between 20-15 kyr BP to a calving front located in Baker Channel towards the east of Larenas Bay at 15 kyr BP (Fig. 1a; Davies et al., 2020).

Between 16.8 – **16.5 cal kyr BP**, the presence of $CaCO_3$, alkenones and marine diatom species (Unit I; Fig. 6) indicate the inflow of marine water into the bay. The relative proportions of $CaCO_3$ and

marine diatom species are particularly low around 16.6 kyr BP, likely due to dilution by an increased supply of glacial sediments. Nonetheless, the marine conditions indicate that the sill at the entrance of the bay (Fig. 2) was submerged and a connection with Baker Channel existed. During this period, relatively coarse (14.89 \pm 6.92 μm) lithogenic material (96.94 \pm 1.02 wt%) rich in icerafted debris dominated the sedimentation in Larenas Bay (Unit I; Fig. 6), indicating the proximity of glacier fronts and/or the remobilization of loose glacial debris left behind by retreating glaciers. Whether these glacial sediments solely originated from the Larenas Bay watershed is uncertain, as surface and tidal currents might have caused the inflow of icebergs and suspended sediments from Baker Channel (Figs. 2 and 7a).

Between 16.5 – **9.1 cal kyr BP**, the absence of $CaCO_3$ (Fig. 6) indicates that marine water was unable to enter the bay, probably due to an emerged or shallow sill at its entrance (Fig. 2). Moreover, the alkenone content remained low, and the proportion of freshwater diatoms increased (10 - 30%) between 16.5 - 12.4 cal kyr BP and prevailed (60 - 90%) between 12.4 - 9.1 cal kyr BP (units II and III; Fig. 6). This evolution of the salinity indicators attests for the gradual freshening of the bay. Furthermore, a considerable sedimentation rate decrease from 9.6 to 0.1 mm/yr occurred near 16.5 cal kyr BP (Fig. 6), likely reflecting a marked change in sediment supply, source(s), and/or erosional processes. As this was a period of regional deglaciation (Davies et al., 2020), this decrease in sedimentation rate might have resulted from the disappearance of glaciers within the Larenas Bay watershed, and/or the development of (proglacial) lakes actively trapping sediments upstream (Piret et al., 2021. Fig. 1b). However, it is unlikely that such environmental changes induced this marked change in sediment accumulation (Antoniazza and Lane, 2021; Piret et al., 2021), and that they occurred simultaneously with the freshening of the bay. This considerable decrease in sedimentation rate might, however, not be related to changes in local sediment supply, i.e., from the Larenas Bay watershed, but to the reduced supply of sediments from the calving front in Baker Channel (Fig. 1a). An additional, and most likely, explanation is the emergence of the sill at the entrance of the bay. This would have blocked the inflow of turbid hypopycnal plumes, and possibly icebergs, from Baker Channel (Fig. 7b), which is supported by the decrease in the amount of lithogenic particles >150 µm (Fig. 6). Such a cut-off could explain the rapid decrease in sedimentation rate as the retreating Patagonian Ice Sheet released large amounts of sediment (e.g., Bertrand et al., 2017; Caniupán et al., 2011; Siani et al., 2010).

From 15.8 cal kyr BP onwards, the accumulation rate of terrestrial organic carbon in Larenas Bay increased continuously, with a culmination at 10.7 cal kyr BP (Fig. 6). This trend most probably reflects the colonization of the recently deglaciated land by *Nothofagus* species (Fig. 1b; Ashworth et al., 1991). The absence of lithogenic particles >150 μm and decreasing mean grain size (10.61 \pm 4.84 μm) between 10.7 - 9.1 cal kyr BP (Fig. 6) indicate that this forest expansion resulted in the stabilization of the landscape, and less debris being washed into Larenas Bay.

Between 9.1 – **1.4 cal kyr BP**, the connection with Baker Channel was re-established as the relative abundance of CaCO₃, marine diatom species and alkenones (Unit IV; Fig. 6) indicate the inflow of marine water in the bay. In addition, the sedimentation rate increased from 0.3 to 0.7 mm/yr, but the stable accumulation rate of terrestrial organic carbon suggests that local sediment input from the Larenas Bay watershed remained relatively constant during the Holocene (Fig. 6). Therefore, we infer that this sedimentation rate increase resulted from the inflow of sediments from Baker Channel, which are mostly lithogenic (88.3 \pm 7.2 wt%) and have a minor organic matter content (1.9 \pm 1.2 wt%) of mainly marine origin (73.0 \pm 7.7%; Rebolledo et al., 2019). This restored

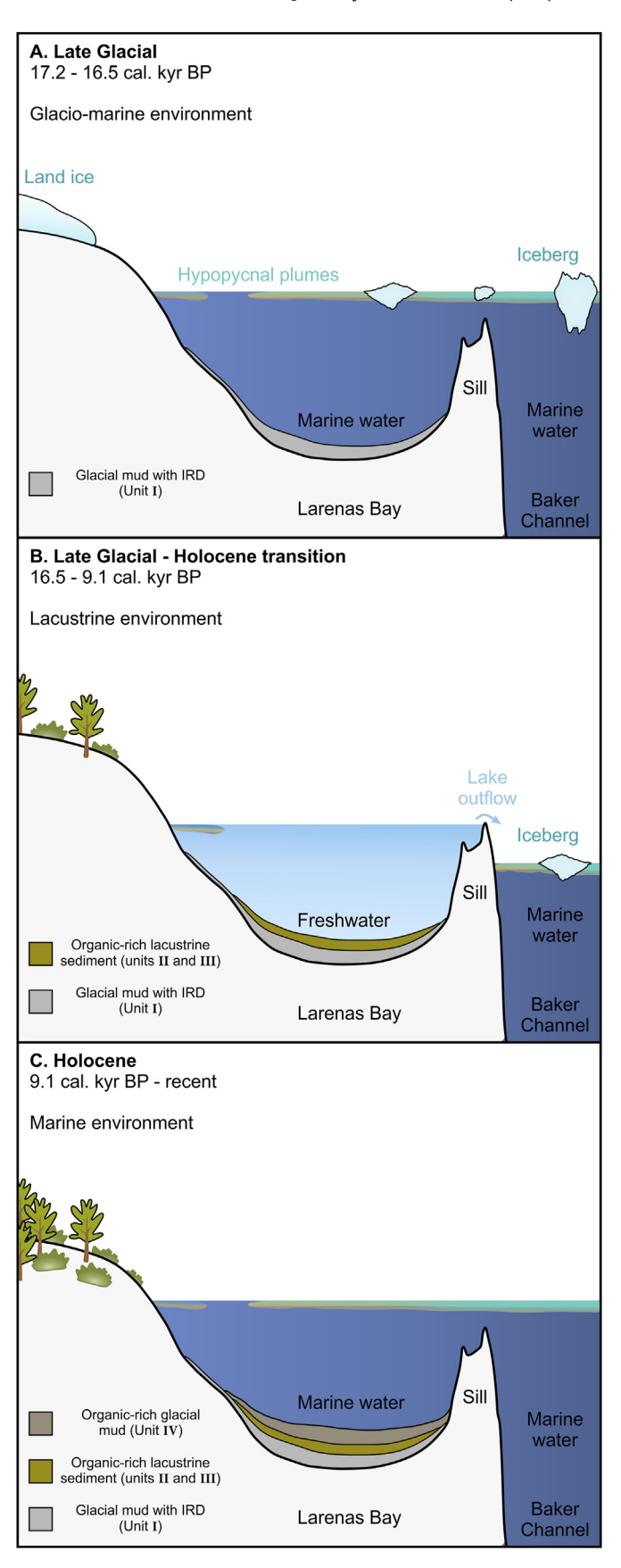


Fig. 7. Graphical interpretation of the paleoenvironmental evolution of Larenas Bay based on the geochemical, physical, and paleoecological parameters presented in Figs. 4 and 6.

inflow of marine water and lithogenic sediments indicates that relative sea-level rise resulted in the submergence of the sill at the entrance of Larenas Bay (Fig. 7c). Compared to the marine-to-lacustrine transition at 16.5 cal kyr BP, this lacustrine-to-marine transition at 9.1 cal kyr BP seems more abrupt, however, it's uncertain whether this relates to the response and/or preservation of the salinity indicators or to a real acceleration in the rate of relative sea-level change.

Between 1.4 – **0.3 cal kyr BP**, the absence of CaCO₃ suggests that marine waters were unable to enter Larenas Bay (Fig. 6). However, the presence of marine diatom species and alkenones imply that the freshening of the bay was limited and saline conditions remained. Moreover, the turbid hypopycnal plume from Baker Channel was still able to enter Larenas Bay, as no apparent change in sedimentation rate occurred (Fig. 6). This restricted marine inflow likely resulted from a submerged but shallow sill, i.e., above its current level (<7.4 m; Fig. 2), at the entrance of the bay.

5.4. Glacial isostatic adjustment

The interplay between eustasy, tectonic movement, and isostasy controlled the evolution of the Larenas Bay environment during the Late Glacial and Holocene. More specifically, our paleoenvironmental reconstruction of Larenas Bay reveals that the sill at the connection with Baker Channel reached sea level at 16.5 cal kyr BP, resulting in the isolation of the bay, and then at 9.1 cal kyr BP, causing marine ingression (Fig. 7). From this, we infer that the post-LGM uplift started before 16.5 cal kyr BP and that it outpaced global sea-level rise until slightly before 9.1 cal kyr BP. The magnitude and rate of this uplift can be reconstructed by comparing the paleoenvironmental evolution of Larenas Bay, represented by the CaCO₃ content of the LAR sediment core, with global sea-level variations (Fig. 8; Lambeck et al., 2014). As global sea level rose ca. 96 m between 16.5 – 9.1 cal kyr BP, Larenas Bay must have risen an equal amount, at an average rate of 1.3 cm/yr, to have remained isolated from Baker Channel (Fig. 8). This isolation ended at 9.1 cal kyr BP (Fig. 7), when eustatic sea level outpaced the uplift. Since then, global sea level rose by ca. 27 m (Fig. 8; Lambeck et al., 2014). The current depth of the sill (7.4 m) indicates that uplift continued during the remainder of the Holocene (ca. 20 m) but at a slower average pace (0.2 cm/yr) relative to global sea-level rise (Fig. 8).

Differentiating the contributions of glacial isostatic adjustment and vertical tectonic movements to these post-LGM uplift rates is challenging as quantitative data on Quaternary tectonic uplift rates are almost inexistent. However, many authors assume that tectonic uplift rates are multiple orders of magnitude slower, and thus negligible, compared to glacial isostatic adjustment rates (e.g., Bourgois et al., 2016; Dietrich et al., 2010; Ivins and James, 1999). Dietrich et al. (2010), who analyzed crustal uplift across the northeastern edge of the Southern Patagonian Icefield between 2003 and 2006, assumed that tectonic uplift rates did not exceed 2 mm/yr. Extrapolating this rate over the last 16.5 kyr would yield a tectonic uplift up to 33 m. However, for the wider region of Larenas Bay, this is most likely a vast overestimation as Georgieva et al. (2016) speculated that the anomalously low elevation of the Baker-Martínez fjord system is not only the result of glacial erosion, but, also of extensional subsidence. This assessment indicates that tectonic uplift during the last 16.5 kyr in the region of Larenas Bay was close to zero or maybe even negative. Therefore, we assume that the uplift rates presented in Fig. 8 mostly represent glacial isostatic adjustment.

The glacial isostatic adjustment signal observed in the Larenas Bay record could be contaminated by postglacial reactivation of local fault systems. Such tectonic activity has been observed in the Strait of Magellan by Bentley and Mcculloch (2005) where the

Puerto del Hambre peat bog downfaulted at least 30 m during the early Holocene. However, there is no sign of seismic activity in the sediment core and sub-bottom profiles of Larenas Bay. Furthermore, the evidence of postglacial fault reactivation in the wider region of Larenas Bay is limited and ambiguous. Both the presence of local fault systems (Georgieva et al., 2016; Glasser and Ghiglione. 2009: SERNAGEOMIN, 2003) and the seismic origin of a 6 kyr turbidite deposited in parts of Baker Channel remain uncertain (Piret et al., 2018). The mass transport deposit observed in Larenas Bay (Fig. 5a) can be subjected to the same scrutiny. In addition, multiple studies suggest that fault activity in the region of the Southern Patagonian Icefield ended in the Pliocene (e.g., Fosdick et al., 2011; Ghiglione et al., 2009; Giacosa et al., 2012; Kraemer, 1998). Lastly, seismic activity between 1900 and 2013 related to the Antarctic/South America plate convergence zone, located ca. 180 km west of Larenas Bay, was low compared to other regions along the Chilean coastline (Hayes et al., 2015). From this lack of evidence indicating seismic activity in and around Larenas Bay, we infer that postglacial fault activity had a negligible influence on its record

5.5. Temporal variations in glacial isostatic adjustment

According to our Larenas Bay record, the average glacial isostatic adjustment rate near the center of the former Patagonian Ice Sheet was 1.3 cm/yr between 16.5 - 9.1 cal kyr BP. It may however not have been as stable as this average suggests (Fig. 8). A stable uplift rate of 1.3 cm/vr would have resulted in a submerged sill and marine inflow into Larenas Bay between 16 - 14.7 and 14.2 -11.8 cal kyr BP (Fig. 8). Yet, the stable sedimentation rate and absence of CaCO₃ indicate that Larenas Bay remained isolated from Baker Channel during the entire 16.5 - 9.1 cal kyr BP period (Fig. 6). Besides, periods of glacier advance/stabilization between 14.1 - 13and 11.4 - 9.3 cal kyr BP might have suppressed isostatic uplift (Fig. 8). Therefore, we suggest that most of the glacial isostatic adjustment must have predated the rapid global sea-level rise corresponding to meltwater pulse 1A (14.5 – 14.0 kyr BP; Fig. 8; Lambeck et al., 2014), which is necessary to maintain freshwater conditions in Larenas Bay. This implies a relatively rapid response of the local solid earth to ice unloading, which is in agreement with independent modelling studies investigating contemporary uplift (Lange et al., 2014). Furthermore, the considerable peak in both the CaCO₃ (>2 wt%) and alkenone (>550 ng/g) contents, and thus marine influence (Aracena et al., 2015; Ríos et al., 2020), between 7.7 - 6.9 cal kyr BP (Fig. 8) suggests that the sill at the entrance of Larenas Bay reached its maximum depth of the last 16.5 kyr. Since global sea-level rise was slowing down during this period (Fig. 8), this maximum relative sill depth indicates that rebound rates had already dropped significantly, which means that most of the post-LGM glacial isostatic adjustment was completed by 7.7 cal kyr BP.

A similar reasoning is valid for the average glacial isostatic adjustment rate (0.2 cm/yr) of the last 9.1 kyr. The high CaCO₃ and alkenone contents between 8.7 – 1.7 cal kyr BP (Figs. 6 and 8) indicate that the residual glacial isostatic uplift had little impact on marine inflow in Larenas Bay. During this time interval, the superimposed high-frequency variations suggest that bioproductivity reacted to changes in climate, thermohaline conditions and nutrient availability (Aracena et al., 2015; Ríos et al., 2020, Figs. 6 and 8). This changed drastically from 1.4 cal kyr BP onwards as the absence of CaCO₃ indicates a restricted inflow of marine waters (Figs. 6 and 8). This decrease in marine influence might have resulted from a combination of decelerated global sea-level rise (Lambeck et al., 2014) and accelerated glacial isostatic uplift in response to glacier recession from their Neoglacial maxima (Fig. 8; Aniya, 2013; Davies et al., 2020). More specifically, this acceleration

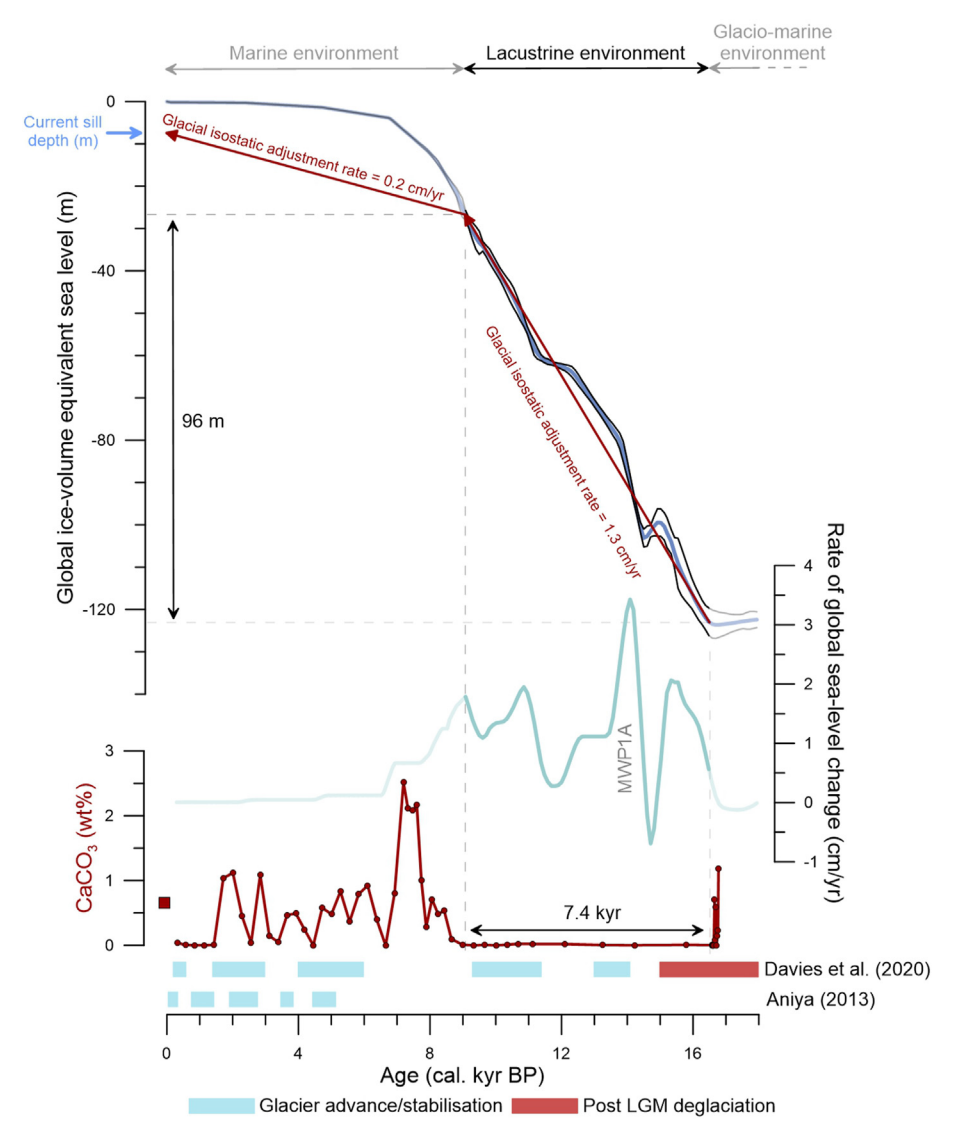


Fig. 8. Comparison of the paleoenvironmental evolution of Larenas Bay, represented by the CaCO₃ content of the LAR sediment core and modern sediment sample (indicated by the square symbol), with global sea level (Lambeck et al., 2014) and local records of glacier dynamics (Aniya, 2013; Davies et al., 2020). Glacial isostatic adjustment rates were inferred from this comparison. The current sill depth at the inlet of Larenas Bay is 7.4 m (Fig. 2). The ages of Aniya (2013) were recalibrated using OxCal and the SHCal20 calibration curve (Hogg et al., 2020). MWP1A = Meltwater Pulse 1A. LGM = Last Glacial Maximum.

seems to have mostly occurred after Neoglaciation III (2780 -1910 cal yr BP; ages calibrated from Aniya, 2013 using SHCal20), and may therefore represent isostatic uplift due to the recession of glaciers on both the Northern and Southern Patagonian Icefields after this particularly extended Neoglacial advance (Bertrand et al., 2012a; Harrison et al., 2008; Mercer, 1982; Siani et al., 2010; Strelin et al., 2014). This paleoenvironmental reconstruction implies that (1) during most of the last 9.1 kyr glacial isostatic adjustment was relatively slow, and (2) that glacial isostatic adjustment accelerated during the late Holocene in response to Neoglacial ice load changes. This idea is supported by the numerical predictions of Ivins and James (2004), which suggest recent rebound rates of 0.3 -1.5 cm/yr around Larenas Bay in response to Neoglacial ice load changes of the Northern and Southern Patagonian Icefields. Moreover, these might represent minimal rebound rates since Ivins and James (2004) likely overestimated local mantle viscosity (Lange et al., 2014; Richter et al., 2016). Furthermore, the relatively high CaCO₃ content of the modern sediment sample (0.66 wt%; Figs. 6 and 8) indicates that (1) this late Holocene acceleration in glacial isostatic adjustment ended somewhere in the last $0.3\,$ kyr, most likely in response to glacier advance during the Little Ice Age chronozone (Fig. 8), and (2) that the glacial isostatic adjustment rates of $1.4-0.3\,$ cal kyr BP, i.e., during the second part of the Neoglacial, were likely faster than those observed today (Lenzano et al., 2021; Richter et al., 2016).

5.6. Spatial variations in glacial isostatic adjustment

To investigate the spatial variations in post-LGM glacial isostatic rebound across Patagonia, we compared the average rates from Larenas Bay to the ones observed east of the Northern Patagonian Icefield (46 – 47.5°S; Bourgois et al., 2016), near the Gran Campo Nevado Icefield (53°S; Kilian et al., 2007) and in the Strait of Magellan (52°S; Ríos et al., 2020, Fig. 9). East of the Northern Patagonian Icefield, within the Lake General Carrera basin, the average glacial isostatic adjustment rate of the last 7.9 kyr (1.5 – 3.4 cm/yr; Bourgois et al., 2016) is about one order of magnitude higher compared to what is observed over the past 9.1 kyr in

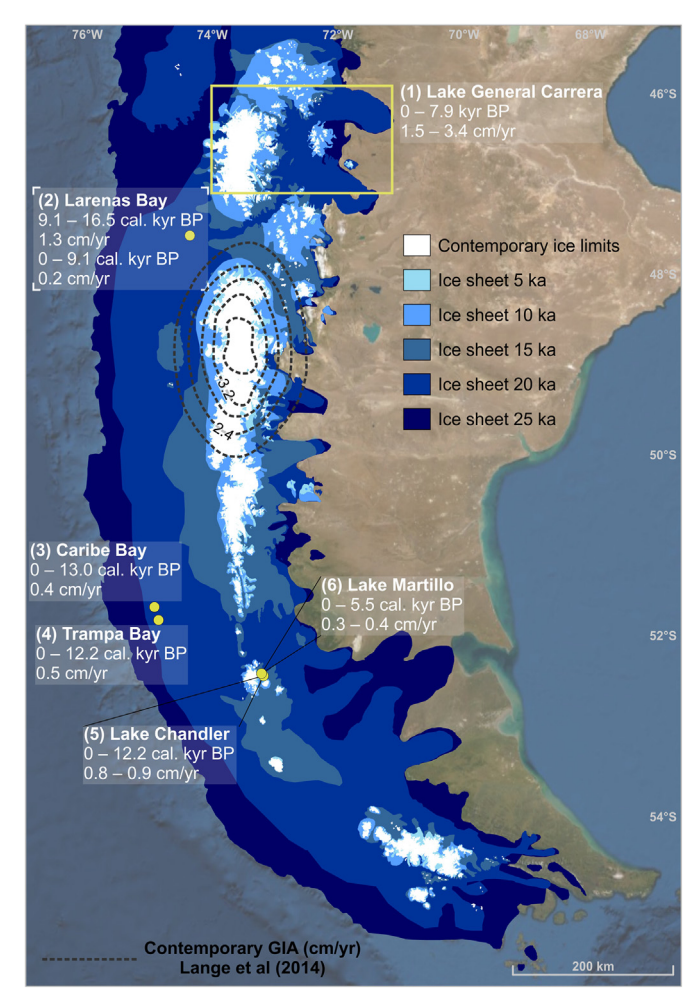


Fig. 9. Compilation of the currently available reconstructions of glacial isostatic adjustment across Patagonia superimposed on a map of the post-Last Glacial Maximum ice sheet evolution (Davies et al., 2020). (1) Lake General Carrera basin (Bourgois et al., 2016), (2) Larenas Bay (this study), (3) Caribe Bay (Ríos et al., 2020), (4) Trampa Bay (Ríos et al., 2020), (5) Lake Chandler (Kilian et al., 2007), and (6) Lake Martillo (Kilian et al., 2007), Note that the glacial isostatic adjustment rates of the Caribe and Trampa bays and Chandler and Martillo lakes were not reported as such by Kilian et al. (2007) and Ríos et al. (2020), but were calculated by comparing the ages of their marine transgression or basin isolation, respectively, to the global sea-level curve from Lambeck et al. (2014). The dashed contour lines indicate contemporary (1996 – 2012) Glacial Isostatic Adjustment (GIA; in cm/yr) derived from GPS observations (Lange et al., 2014).

Larenas Bay (0.2 cm/yr; Fig. 9). This difference probably relates to a local rebound acceleration in response to (1) recession of the General Carrera outlet lobe from its 7.9 ± 1.1 kyr BP and 10.9 ± 1.3 kyr BP moraines (Bourgois et al., 2016), and (2) major drainage events of Lake General Carrera (Thorndycraft et al., 2019). In southern Patagonia (53°S), Kilian et al. (2007) observed a similar evolution in glacial isostatic adjustment in the area of lakes Chandler and Martillo to what is oberserved in the Larenas Bay record, i.e., faster rebound rates (>1 cm/yr) during the Late Glacial — Holocene transition compared to the mid and late Holocene (0.3 — 0.4 cm/yr). In the western Strait of Magellan, the Caribe and Trampa Bay records reveal a decrease in post-LGM glacial isostatic rebound to \leq 0.5 cm/yr towards the western edge of the former Patagonian Ice Sheet (Fig. 9; Ríos et al., 2020).

Recognizing regional trends in post-LGM glacial isostatic adjustment across the area formerly covered by the Patagonian Ice Sheet is currently difficult as the number of records is low and their

temporal resolution is limited and variable. In addition, the Holocene rebound rates of Larenas Bay and lakes Chandler, Martillo and General Carrera were probably affected by Neoglacial advances (Aniya, 2013; Klemann et al., 2007; Koch and Kilian, 2005) whereas those from the Caribe and Trampa bays were further away from the 5 ka ice margin (Davies et al., 2020) and therefore likely more stable during the Holocene. Spatial variability in glacial isostatic adjustment is better captured by GPS observations, which reveal a domelike spatial distribution of contemporary glacial isostatic adjustment centered around the northern sector of the Southern Patagonian Icefield ($48.5 - 49.5^{\circ}$ S; Fig. 9; Lange et al., 2014), but, these observations are not suited to extrapolate over the former extend of the Patagonian Ice Sheet. Moreover, spatial variations in lithosphere and mantle rheology might also have led to local variations in glacial isostatic rebound that are independent of ice margin position (Richter et al., 2016). Finally, the possibility of postglacial fault reactivation contaminating local glacial isostatic adjustment observations should not be neglected (Bentley and Mcculloch, 2005; Georgieva et al., 2016). Additional glacial isostatic adjustment reconstructions from both sides of the Andes are therefore needed to better capture possible spatiotemporal variations in rebound rates.

6. Conclusion

Our multi-proxy reconstruction of the paleoenvironmental evolution of Larenas Bay provides new data on the deglaciation of the Baker-Martínez fjord system and postglacial isostatic adjustment near the center of the former Patagonian Ice Sheet. Results indicate that Larenas Bay was deglaciated prior to 17.2 kyr BP. Marine conditions prevailed until 16.5 cal kyr BP and after 9.1 cal kyr BP, but the bay was isolated from Baker Channel inbetween. Assuming a negligible impact of tectonic uplift and postglacial fault reactivation, we infer that the postglacial rebound started before 16.5 cal kyr BP and that it outpaced global sea-level rise until slightly before 9.1 cal kyr BP. Between 16.5 - 9.1 cal kyr BP, the center of the former Patagonian Ice Sheet rose ca. 96 m, at an average rate of 1.3 cm/yr. Glacial isostatic adjustment continued (ca. 20 m) over the last 9.1 kyr, but at a slower average pace of 0.2 cm/yr. By comparing multi-millennial variations in our salinity indicators with existing records of global sea-level rise, we suggest that the glacial isostatic adjustment rate also fluctuated within these time intervals, in response to glacier dynamics. More specifically, most of the glacial isostatic adjustment registered between 16.5 9.1 cal kyr BP seems to have occurred before meltwater pulse 1A (14.5 - 14.0 kyr BP). Likewise, it appears that the highest glacial isostatic rebound rates of the last 9.1 kyr occurred during the late Holocene, most likely in response to glacier recession from their Neoglacial maxima. This implies a relatively rapid response of the local solid earth to ice unloading, which agrees with independent modelling studies investigating contemporary uplift. The compilation of the currently available paleorecords of glacial isostatic adjustment across Patagonia does not allow us to identify regional trends in post-LGM rebound as the number of records is low and their temporal resolution is limited and variable. We conclude that the center of the former Patagonian Ice Sheet experienced a glacial isostatic adjustment of ca. 116 m over the last 16.5 kyr, and that >80% occurred during the Late Glacial and early Holocene.

Author contributions statement

MT analyzed the LAR core for bulk organic geochemistry, grain size, and biogenic silica, carbonate and lithogenic content, processed the data, interpreted the results, and wrote the manuscript. SB obtained funding, coordinated the collaborative research

activities, and wrote the manuscript with MT. CL obtained funding, and assisted PC with diatom identification and ecological interpretation. PC performed the microscopy analysis of diatoms and their paleoecological classification. HA took the core pictures, scanned the LAR core for magnetic susceptibility and sampled the LAR core. SPG obtained funding and supervised the alkenone analysis. RdeP was in charge of the radiocarbon analyses at UCI. RK^{\dagger} collected the seismic data and sediment core from Larenas Bay. All authors, except RK^{\dagger} , contributed to the interpretation of the results and to the writing of the manuscript, and approved the final version.

Declaration of competing interest

The authors hereby declare that the submitted work was not carried out in the presence of any personal, professional or financial relationships that could potentially be construed as a conflict of interest.

Acknowledgements

This research was funded by Ghent University (BOF project 01D30018), FONDAP COPAS (project #150100007), FONDAP IDEAL (project #15150003), and COPAS Sur-Austral (ANID APOYO CCTE AFB170006). Matthias Troch was supported by a Ghent University BOF PhD fellowship (01D30018). We thank Marcelo Arévalo and the captain and crew of the R/V Gran Campo II and R/V Sur-Austral for their help during the seismic survey, sediment coring and CTD profiling. We are grateful to Diego Narvaez and Nicolas Mayorga for acquiring and processing the CTD data. We acknowledge Veerle Vandenhende for operating the ICP-AES and Victor Acuña for the analysis of the alkenones. We thank Juliane Mueller for providing the alkenone retention times of Emiliania huxleyi cultures. Francisco Ríos and Marcelo Arévalo kindly facilitated access to the R/V Gran Campo II cruise data. We thank Stijn Albers and Katleen Wils for their help with the processing and interpretation of the seismic data and Giuseppe Siani for looking into the composition of the detrital layers. Special thanks go to Loïc Piret for constructive discussions and for providing valuable suggestions on an earlier version of this manuscript. The authors also wish to thank Bethan Davies and an anonymous reviewer for their constructive comments and feedback. This article is dedicated to the memory of our colleague and friend Rolf Kilian, and is a contribution to the Study Group "Atmosphere-ocean changes in the Southeast Pacific — from glacial/interglacial to instrumental time-scales" of the Hanse-Wissenschaftskolleg (Delmenhorst, Germany). The dataset presented in this article is available on PANGAEA at https://doi.org/10. 1594/PANGAEA.937823.

Appendix A. Supplementary data

Supplementary data to this article can be found online at https://doi.org/10.1016/j.quascirev.2021.107346.

References

- Aiken, C.M., 2012. Seasonal thermal structure and exchange in Baker Channel, Chile.

 Dynam. Atmos. Oceans 58, 1–19. https://doi.org/10.1016/j.dynatmoce.2012.07.001.
- Aniya, M., 2013. Holocene glaciations of hielo patagónico (Patagonia icefield), south America: a brief review. Geochem. J. 47, 97–105.
- Antoniazza, G., Lane, S.N., 2021. Sediment yield over glacial cycles: a conceptual model. Progress in Physical Geography: Earth and Environment 030913332199729. https://doi.org/10.1177/0309133321997292.
- Aracena, C., Kilian, R., Lange, C.B., Bertrand, S., Lamy, F., Arz, H.W., De Pol-Holz, R., Baeza, O., Pantoja, S., Kissel, C., 2015. Holocene variations in productivity associated with changes in glacier activity and freshwater flux in the central

- basin of the Strait of Magellan. Palaeogeogr. Palaeoclimatol. Palaeoecol. 436, 112–122. https://doi.org/10.1016/j.palaeo.2015.06.023.
- Ashworth, A.C., Markgraf, V., Villagran, C., 1991. Late Quaternary climatic history of the Chilean Channels based on fossil pollen and beetle analyses, with an analysis of the modern vegetation and pollen rain. J. Quat. Sci. 6, 279–291. https://doi.org/10.1002/jqs.3390060403.
- Balascio, N.L., Zhang, Z., Bradley, R.S., Perren, B., Dahl, S.O., Bakke, J., 2011. A multi-proxy approach to assessing isolation basin stratigraphy from the Lofoten Islands, Norway. Quat. Res. 75, 288–300. https://doi.org/10.1016/j.yqres.2010.08.012.
- Bendle, J.A.P., Rosell-Melé, A., Cox, N.J., Shennan, I., 2009. Alkenones, alkenoates, and organic matter in coastal environments of NW Scotland: assessment of potential application for sea level reconstruction. G-cubed 10. https://doi.org/10.1029/2009GC002603.
- Benn, D.I., Evans, D.J.A., 2010. Glaciers and Glaciation, second. Hodder education, London.
- Bentley, M.J., Mcculloch, R.D., 2005. Impact of neotectonics on the record of glacier and sea level fluctuations, strait of magellan, southern Chile. Geogr. Ann. Phys. Geogr. 87, 393—402. https://doi.org/10.1111/j.0435-3676.2005.00265.x.
- Bertrand, S., Hughen, K.A., Lamy, F., Stuut, J.B., Torrejon, F., Lange, C.B., 2012a. Precipitation as the main driver of neoglacial fluctuations of gualas glacier, northern patagonian icefield. Clim. Past 8, 519–534. https://doi.org/10.5194/cp-8-519-2012.
- Bertrand, S., Hughen, K.A., Sepúlveda, J., Pantoja, S., 2012b. Geochemistry of surface sediments from the fjords of Northern Chilean Patagonia (44–47°S): spatial variability and implications for paleoclimate reconstructions. Geochem. Cosmochim. Acta 76, 125–146. https://doi.org/10.1016/j.gca.2011.10.028.
- Bertrand, S., Lange, C.B., Pantoja, S., Hughen, K., Van Tornhout, E., Wellner, J.S., 2017. Postglacial fluctuations of Cordillera Darwin glaciers (southernmost Patagonia) reconstructed from Almirantazgo fjord sediments. Quat. Sci. Rev. 177, 265–275. https://doi.org/10.1016/j.quascirev.2017.10.029.
- Blaauw, M., Christen, J.A., 2011. Flexible paleoclimate age-depth models using an autoregressive gamma process. Bayesian Analysis 6, 457–474. https://doi.org/ 10.1214/11-BA618.
- Bligh, E.G., Dyer, W.J., 1959. A rapid method of total lipid extraction and purification. Can. J. Biochem. Physiol. 37, 911–917. https://doi.org/10.1139/o59-099.
- Blott, S.J., Pye, K., 2001. Gradistat: a grain size distribution and statistics package for the analysis of unconsolidated sediments. Earth Surf. Process. Landforms 26, 1237–1248.
- Bourgois, J., Cisternas, M.E., Braucher, R., Bourlès, D., Frutos, J., 2016. Geomorphic records along the general Carrera (Chile)—Buenos Aires (Argentina) glacial lake (46°–48°S), climate inferences, and glacial rebound for the past 7–9 ka. J. Geol. 124, 27–53. https://doi.org/10.1086/684252.
- Bromwich, D.H., Nicolas, J.P., 2010. Ice-sheet uncertainty. Nat. Geosci. 3, 596–597. https://doi.org/10.1038/ngeo946.
- Caniupán, M., Lamy, F., Lange, C.B., Kaiser, J., Arz, H., Kilian, R., Baeza Urrea, O., Aracena, C., Hebbeln, D., Kissel, C., Laj, C., Mollenhauer, G., Tiedemann, R., 2011. Millennial-scale sea surface temperature and Patagonian Ice Sheet changes off southernmost Chile (53°S) over the past ~60 kyr. Paleoceanography 26. https://doi.org/10.1029/2010PA002049 n/a-n/a.
- Carter, S.J., Colman, S.M., 1994. Biogenic silica in lake baikal sediments: results from 1990-1992 American cores. J. Great Lake. Res. 20, 751–760. https://doi.org/ 10.1016/S0380-1330(94)71192-8.
- Cembrano, J., Lavenu, A., Reynolds, P., Arancibia, G., López, G., Sanhueza, A., 2002. Late Cenozoic transpressional ductile deformation north of the Nazca–South America–Antarctica triple junction. Tectonophysics 354, 289–314. https://doi.org/10.1016/S0040-1951(02)00388-8.
- Chen, C., Millero, F.J., 1977. Speed of sound in seawater at high pressures. J. Acoust. Soc. Am. 62, 1129–1135. https://doi.org/10.1121/1.381646.
- Clark, P.U., Tarasov, L., 2014. Closing the sea level budget at the last glacial maximum. Proc. Natl. Acad. Sci. Unit. States Am. 111, 15861–15862. https://doi.org/10.1073/pnas.1418970111.
- DaSilva, J.L., Anderson, J.B., Stravers, J., 1997. Seismic facies changes along a nearly continuous 24° latitudinal transect: the fjords of Chile and the northern Antarctic Peninsula. Mar. Geol. 143, 103–123. https://doi.org/10.1016/S0025-3227(97)00092-3
- Davies, B.J., Darvill, C.M., Lovell, H., Bendle, J.M., Dowdeswell, J.A., Fabel, D., García, J.-L., Geiger, A., Glasser, N.F., Gheorghiu, D.M., Harrison, S., Hein, A.S., Kaplan, M.R., Martin, J.R.V., Mendelova, M., Palmer, A., Pelto, M., Rodés, Á., Sagredo, E.A., Smedley, R.K., Smellie, J.L., Thorndycraft, V.R., 2020. The evolution of the Patagonian Ice Sheet from 35 ka to the present day (PATICE). Earth Sci. Rev. 204, 103152. https://doi.org/10.1016/j.earscirev.2020.103152.
- Dietrich, R., Ivins, E.R., Casassa, G., Lange, H., Wendt, J., Fritsche, M., 2010. Rapid crustal uplift in Patagonia due to enhanced ice loss. Earth Planet Sci. Lett. 289, 22–29. https://doi.org/10.1016/j.epsl.2009.10.021.
- Dlabola, E.K., Wilson, G.S., Gorman, A.R., Riesselman, C.R., Moy, C.M., 2015. A post-glacial relative sea-level curve from Fiordland, New Zealand. Global Planet. Change 131, 104—114. https://doi.org/10.1016/j.gloplacha.2015.05.010.
- Dowdeswell, J.A., Vásquez, M., 2013. Submarine landforms in the fjords of southern Chile: implications for glacimarine processes and sedimentation in a mild glacier-influenced environment. Quat. Sci. Rev. 64, 1–19. https://doi.org/10.1016/j.quascirev.2012.12.003.
- Fosdick, J.C., Romans, B.W., Fildani, A., Bernhardt, A., Calderon, M., Graham, S.A., 2011. Kinematic evolution of the Patagonian retroarc fold-and-thrust belt and Magallanes foreland basin, Chile and Argentina, 51 30'S. Geol. Soc. Am. Bull. 123,

- 1679-1698. https://doi.org/10.1130/B30242.1.
- Garreaud, R., Lopez, P., Minvielle, M., Rojas, M., 2013. Large-scale control on the patagonian climate. J. Clim. 26, 215–230. https://doi.org/10.1175/JCLI-D-12-000011
- Garrett, E., Melnick, D., Dura, T., Cisternas, M., Ely, L.L., Wesson, R.L., Jara-Muñoz, J., Whitehouse, P.L., 2020. Holocene relative sea-level change along the tectonically active Chilean coast. Quat. Sci. Rev. 236, 106281. https://doi.org/10.1016/ j.quascirev.2020.106281.
- Georgieva, V., Melnick, D., Schildgen, T.F., Ehlers, T.A., Lagabrielle, Y., Enkelmann, E., Strecker, M.R., 2016. Tectonic control on rock uplift, exhumation, and topography above an oceanic ridge collision: southern Patagonian Andes (47°S), Chile. Tectonics 35, 1317–1341. https://doi.org/10.1002/2016TC004120.
- Ghiglione, M.C., Suarez, F., Ambrosio, A., Poian, G.D. a, Cristallini, E.O., Pizzio, M.F., Reinoso, R.M., 2009. Structure and evolution of the austral basin fold-thrust belt, southern patagonian Andes. Rev. Asoc. Geol. Argent. 65, 215–226.
- Giacosa, R., Fracchia, D., Heredia, N., 2012. Structure of the southern patagonian Andes at 49°S, Argentina. Geol. Acta 10, 265–282. https://doi.org/10.1344/105.000001749.
- Glasser, N.F., Ghiglione, M.C., 2009. Structural, tectonic and glaciological controls on the evolution of fjord landscapes. Geomorphology 105, 291–302. https:// doi.org/10.1016/j.geomorph.2008.10.007.
- González, H.E., Castro, L.R., Daneri, G., Iriarte, J.L., Silva, N., Tapia, F., Teca, E., Vargas, C.A., 2013. Land-ocean gradient in haline stratification and its effects on plankton dynamics and trophic carbon fluxes in Chilean Patagonian fjords (47-50°S). Prog. Oceanogr. 119, 32–47. https://doi.org/10.1016/j.pocean.2013.06.003.
- Harrison, S., Glasser, N., Winchester, V., Haresign, E., Warren, C., Duller, G.A.T., Bailey, R., Ivy-Ochs, S., Jansson, K., Kubik, P., 2008. Glaciar León, Chilean Patagonia: late-holocene chronology and geomorphology. Holocene 18, 643–652. https://doi.org/10.1177/0959683607086771.
- Hayes, G.P., Smoczyk, G.M., Benz, H.M., Villaseñor, A., Furlong, K.P., 2015. Seismicity of the Earth 1900–2013, Seismotectonics of South America (Nazca Plate Region): U.S. Geological Survey Open-File Report 2015–1031-E, 1 Sheet, Scale 1:14 000 000. https://doi.org/10.3133/of20151031E.
- Heaton, T.J., Köhler, P., Butzin, M., Bard, E., Reimer, R.W., Austin, W.E.N., Bronk Ramsey, C., Grootes, P.M., Hughen, K.A., Kromer, B., Reimer, P.J., Adkins, J., Burke, A., Cook, M.S., Olsen, J., Skinner, L.C., 2020. Marine20—the marine radiocarbon age calibration curve (0–55,000 cal BP). Radiocarbon 62, 779–820. https://doi.org/10.1017/RPC.2020.68.
- Hebbein, D., Marchant, M., Freudenthal, T., Wefer, G., 2000. Surface sediment distribution along the Chilean continental slope related to upwelling and productivity. Mar. Geol. 164, 119–137. https://doi.org/10.1016/S0025-3227(99) 00129-2
- Heiri, O., Lotter, A.F., Lemcke, G., 2001. Loss on ignition as a method for estimating organic and carbonate content in sediments: reproducibility and comparability of results. J. Paleolimnol. 25, 101–110. https://doi.org/10.1023/A:1008119611481.
- Hodgson, D.A., Whitehouse, P.L., De Cort, G., Berg, S., Verleyen, E., Tavernier, I., Roberts, S.J., Vyverman, W., Sabbe, K., O'Brien, P., 2016. Rapid early Holocene sea-level rise in prydz bay, east Antarctica. Global Planet. Change 139, 128–140. https://doi.org/10.1016/j.gloplacha.2015.12.020.
- Hogg, A.G., Heaton, T.J., Hua, Q., Palmer, J.G., Turney, C.S., Southon, J., Bayliss, A., Blackwell, P.G., Boswijk, G., Bronk Ramsey, C., Pearson, C., Petchey, F., Reimer, P., Reimer, R., Wacker, L., 2020. SHCal20 southern Hemisphere calibration, 0–55,000 Years cal BP. Radiocarbon 62, 759–778. https://doi.org/10.1017/RDC.2020.59.
- Hubbard, A., Hein, A.S., Kaplan, M.R., Hulton, N.R.j., Glasser, N., 2005. A modelling reconstruction of the last glacial maximum ice sheet and its deglaciation in the vicinity of the northern patagonian icefield, south America. Geogr. Ann. Phys. Geogr. 87, 375—391. https://doi.org/10.1111/j.0435-3676.2005.00264.x.
- Ivins, E.R., James, T.S., 2004. Bedrock response to Llanquihue Holocene and present-day glaciation in southernmost South America. Geophys. Res. Lett. 31, L24613. https://doi.org/10.1029/2004GL021500.
- Ivins, E.R., James, T.S., 1999. Simple models for late Holocene and present-day Patagonian glacier fluctuations and predictions of a geodetically detectable isostatic response. Geophys. J. Int. 138, 601–624. https://doi.org/10.1046/j.1365-246x.1999.00899.x.
- Kilian, R., Baeza, O., Steinke, T., Arevalo, M., Rios, C., Schneider, C., 2007. Late Pleistocene to Holocene marine transgression and thermohaline control on sediment transport in the western Magellanes fjord system of Chile (53°S). Quat. Int. 161, 90–107. https://doi.org/10.1016/j.quaint.2006.10.043.
- Klemann, V., Ivins, E.R., Martinec, Z., Wolf, D., 2007. Models of active glacial isostasy roofing warm subduction: case of the South Patagonian Ice Field. J. Geophys. Res. 112, B09405. https://doi.org/10.1029/2006JB004818.
- Koch, J., Kilian, R., 2005. 'Little ice age' glacier fluctuations, gran Campo Nevado, southernmost Chile. Holocene 15, 20–28. https://doi.org/10.1191/0959683605h1780rp.
- Kraemer, P.E., 1998. Structure of the patagonian Andes: regional balanced cross section at 50°S, Argentina. Int. Geol. Rev. 40, 896–915. https://doi.org/10.1080/00206819809465244.
- Lagabrielle, Y., Suárez, M., Rossello, E.A., Hérail, G., Martinod, J., Régnier, M., de la Cruz, R., 2004. Neogene to quaternary tectonic evolution of the patagonian Andes at the latitude of the Chile triple junction. Tectonophysics 385, 211–241. https://doi.org/10.1016/j.tecto.2004.04.023.
- Lambeck, K., Rouby, H., Purcell, A., Sun, Y., Sambridge, M., 2014. sea level and global ice volumes from the last glacial maximum to the Holocene. Proc. Natl. Acad. Sci. Unit. States Am. 111, 15296–15303. https://doi.org/10.1073/pnas.1411762111.

- Lange, H., Casassa, G., Ivins, E.R., Schröder, L., Fritsche, M., Richter, A., Groh, A., Dietrich, R., 2014. Observed crustal uplift near the Southern Patagonian Icefield constrains improved viscoelastic Earth models. Geophys. Res. Lett. 41, 805–812. https://doi.org/10.1002/2013GL058419.
- Lasher, G.E., Axford, Y., Masterson, A.L., Berman, K., Larocca, L.J., 2020. Holocene temperature and landscape history of southwest Greenland inferred from isotope and geochemical lake sediment proxies. Quat. Sci. Rev. 239, 106358. https://doi.org/10.1016/j.quascirev.2020.106358.
- Lenzano, M.G., Rivera, A., Durand, M., Hernandez, J., Vasquez, R., Lenzano, L., Rada, C., 2021. Glacial-isostatic adjustment in the Southern Patagonia Icefield based upon permanent GNSS stations. In: EGU General Assembly 2021, Online, 19–30 Apr 2021, EGU21-13451. https://doi.org/10.5194/egusphere-egu21-13451.
- Long, A.J., Woodroffe, S.A., Roberts, D.H., Dawson, S., 2011. Isolation basins, sea-level changes and the Holocene history of the Greenland Ice Sheet. Quat. Sci. Rev. 30, 3748–3768. https://doi.org/10.1016/j.guascirey.2011.10.013.
- Luebert, F., Pliscoff, P., 2006. Sinopsis bioclimática y vegetacional de Chile. Editorial Universitaria, Santiago.
- Mackie, E.A.V., Lloyd, J.M., Leng, M.J., Bentley, M.J., Arrowsmith, C., 2007. Assessment of δ13C and C/N ratios in bulk organic matter as palaeosalinity indicators in Holocene and Lateglacial isolation basin sediments, northwest Scotland. J. Quat. Sci. 22, 579–591. https://doi.org/10.1002/jqs.1081.
- Marsaglia, K., Milliken, K., Doran, L., 2013. IODP digital reference for smear slide analysis of marine mud. Part 1: methodology and atlas of siliciclastic and volcanogenic components. IODP Technical Note 1. https://doi.org/10.2204/ iodp.tn.1.2013.
- Marsaglia, K., Milliken, K., Leckie, R.M., Tentori, D., Doran, L., 2015. IODP smear slide digital reference for sediment analysis of marine mud. Part 2: methodology and atlas of biogenic components. IODP Technical Note 2. https://doi.org/10.2204/ iodp.tn.2.2015.
- Mazzulio, J., Graham, A.G., 1988. Handbook for Shipboard Sedimentologists Ocean Drilling Program. Texas A&M University. Technical Note No. 8. 67pp.
- Mercer, J.H., 1982. Holocene glacier variations in southern Patagonia. Striae 18, 35–40
- Mortlock, R.A., Froelich, P.N., 1989. A simple method for the rapid determination of biogenic opal in pelagic marine sediments. Oceanogr. Res. Pap. 36, 1415–1426. https://doi.org/10.1016/0198-0149(89)90092-7.
- Nowaczyk, N.R., 2002. Logging of magnetic susceptibility. In: Last, W.M., Smol, J.P. (Eds.), Tracking Environmental Change Using Lake Sediments. Volume 1: Basin Analysis, Coring, and Chronological Techniques. Kluwer Academic Publishers, pp. 155–170.
- Piret, L., Bertrand, S., Hawkings, J., Kylander, M.E., Torrejón, F., Amann, B., Wadham, J., 2021. High-resolution fjord sediment record of a receding glacier with growing intermediate proglacial lake (Steffen Fjord, Chilean Patagonia). Earth Surf. Process. Landforms 46, 239–251. https://doi.org/10.1002/esp.5015.
- Piret, L., Bertrand, S., Kissel, C., De Pol-Holz, R., Tamayo Hernando, A., Van Daele, M., 2018. First evidence of a mid-Holocene earthquake-triggered megaturbidite south of the Chile Triple Junction. Sediment. Geol. 375, 120–133. https:// doi.org/10.1016/j.sedgeo.2018.01.002.
- Piret, L., Troch, M., Vandekerkhove, E., Harada, N., Moffat, C., Rivera, A., Mansilla, R., Bertrand, S., 2019. Gridded bathymetry of the Baker-Martinez fjord complex (Chile, 48°S) v2. Interdisciplinary Earth Data Alliance (IEDA). https://doi.org/ 10.1594/IEDA/324862.
- Praet, N., Moernaut, J., Van Daele, M., Boes, E., Haeussler, P.J., Strupler, M., Schmidt, S., Loso, M.G., De Batist, M., 2017. Paleoseismic potential of sublacustrine landslide records in a high-seismicity setting (south-central Alaska). Mar. Geol. 384, 103–119. https://doi.org/10.1016/j.margeo.2016.05.004.
- Quiroga, E., Ortiz, P., González-saldías, R., Reid, B., Tapia, F.J., Pérez-santos, I., Rebolledo, L., Mansilla, R., Pineda, C., Cari, I., Salinas, N., Montiel, A., Gerdes, D., 2016. Seasonal benthic patterns in a glacial Patagonian fjord: the role of suspended sediment and terrestrial organic matter. Mar. Ecol. Prog. Ser. 561, 31–50. https://doi.org/10.3354/meps11903.
- R Core Team, 2020. R: A Language and Environment for Statistical Computing. R Foundation for Statistical Computing, Vienna, Austria. URL. https://www.R-project.org/.
- Rebolledo, L., Bertrand, S., Lange, C.B., Tapia, F.J., Quiroga, E., Troch, M., Silva, N., Cárdenas, P., Pantoja, S., 2019. Compositional and biogeochemical variations of sediments across the terrestrial-marine continuum of the Baker-Martínez fjord system (Chile, 48°S). Prog. Oceanogr. 174, 89–104. https://doi.org/10.1016/j.pocean.2018.12.004.
- Reynolds, J.M., 2011. An Introduction to Applied and Environmental Geophysics, second ed. Wiley-Blackwell, Chichester, UK.
- Richter, A., Ivins, E., Lange, H., Mendoza, L., Schröder, L., Hormaechea, J.L., Casassa, G., Marderwald, E., Fritsche, M., Perdomo, R., Horwath, M., Dietrich, R., 2016. Crustal deformation across the southern patagonian icefield observed by GNSS. Earth Planet Sci. Lett. 452, 206–215. https://doi.org/10.1016/j.epsl.2016.07.042.
- Ríos, F., Kilian, R., Lange, C.B., Baeza-Urrea, O., Arz, H.W., Zindorf, M., De Pol-Holz, R., Lamy, F., 2020. Environmental and coastline changes controlling Holocene carbon accumulation rates in fjords of the western Strait of Magellan region. Continent. Shelf Res. 199, 104101. https://doi.org/10.1016/j.csr.2020.104101.
- Roe, H.M., Doherty, C.T., Patterson, R.T., Milne, G.A., 2013. Isolation basin records of late Quaternary sea-level change, central mainland British Columbia, Canada. Quat. Int. 310, 181–198. https://doi.org/10.1016/j.quaint.2013.01.026.
- Schlitzer, R., 2021. Ocean Data View v5.4.0. http://odv.awi.de.

- SERNAGEOMIN, 2003. Mapa Geológico de Chile: versión digital. Servicio Nacional de Geología y Minería, Publicación Geológica Digital No. 4, (CD-ROM, versión1.0, 2003). Santiago.
- SHOA, 2001. Servicio Hidrográfico y Oceanográfico de la Armada de Chile, Nautical chart "9100 Canal Baker y Puertos Adyacentes (Canal Baker).
- Siani, G., Colin, C., Michel, E., Carel, M., Richter, T., Kissel, C., Dewilde, F., 2010. Late glacial to Holocene terrigenous sediment record in the northern patagonian margin: paleoclimate implications. Palaeogeogr. Palaeoclimatol. Palaeoecol. 297, 26–36. https://doi.org/10.1016/j.palaeo.2010.07.011.
- Sievers, H.A., Silva, N., 2008. Water masses and circulation in austral Chilean channels and fjords. In: Silva, N., Palma, S. (Eds.), Progress in the Oceanographic Knowledge of Chilean Interior Waters, from Puerto Montt to Cape Horn. Comité Oceanográfico Nacional-Pontificia Universidad Católica de Valparaíso, Valparaíso, pp. 53–58.
- Strelin, J.A., Kaplan, M.R., Vandergoes, M.J., Denton, G.H., Schaefer, J.M., 2014. Holocene glacier history of the Lago Argentino basin, southern patagonian icefield. Quat. Sci. Rev. 101, 124–145. https://doi.org/10.1016/j.quascirev.2014.06.026.
- Thorndycraft, V.R., Bendle, J.M., Benito, G., Davies, B.J., Sancho, C., Palmer, A.P., Fabel, D., Medialdea, A., Martin, J.R.v., 2019. Glacial lake evolution and Atlantic-Pacific drainage reversals during deglaciation of the Patagonian Ice Sheet. Quat. Sci. Rev. 203, 102–127. https://doi.org/10.1016/j.quascirev.2018.10.036.

 Verardo, D.J., Froelich, P.N., McIntyre, A., 1990. Determination of organic carbon and
- Verardo, D.J., Froelich, P.N., McIntyre, A., 1990. Determination of organic carbon and nitrogen in marine sediments using the Carlo Erba NA-1500 analyzer. Deep Sea Research Part A. Oceanogr. Res. Pap. 37, 157–165. https://doi.org/10.1016/0198-

- 0149(90)90034-S.
- Verleyen, E., Tavernier, I., Hodgson, D.A., Whitehouse, P.L., Kudoh, S., Imura, S., Heirman, K., Bentley, M.J., Roberts, S.J., De Batist, M., Sabbe, K., Vyverman, W., 2017. Ice sheet retreat and glacio-isostatic adjustment in Lützow-Holm Bay, East Antarctica. Quat. Sci. Rev. 169, 85–98. https://doi.org/10.1016/j.quascirev.2017.06.003.
- Wang, K., Hu, Y., Bevis, M., Kendrick, E., Smalley, R., Vargas, R.B., Lauría, E., 2007. Crustal motion in the zone of the 1960 Chile earthquake: detangling earthquake-cycle deformation and forearc-sliver translation. G-cubed 8. https://doi.org/10.1029/2007GC001721 n/a-n/a.
- Wang, L., Longo, W.M., Dillon, J.T., Zhao, J., Zheng, Y., Moros, M., Huang, Y., 2019. An efficient approach to eliminate steryl ethers and miscellaneous esters/ketones for gas chromatographic analysis of alkenones and alkenoates. J. Chromatogr. A 1596, 175–182. https://doi.org/10.1016/j.chroma.2019.02.064.
- Whitehouse, P.L., 2018. Glacial isostatic adjustment modelling: historical perspectives, recent advances, and future directions. Earth Surf. Dyn. 6, 401–429. https://doi.org/10.5194/esurf-6-401-2018.
- Wils, K., Van Daele, M., Lastras, G., Kissel, C., Lamy, F., Siani, G., 2018. Holocene event record of Aysén fjord (Chilean Patagonia): an interplay of volcanic eruptions and crustal and megathrust earthquakes. J. Geophys. Res. Solid Earth 123, 324–343. https://doi.org/10.1002/2017/B014573.
- Wunderlich, J., Müller, S., 2003. High-resolution sub-bottom profiling using parametric acoustics. Int. Ocean Syst. 7, 6–11.